Continental Shelf Research 173 (2019) 27–42

Contents lists available at ScienceDirect

Continental Shelf Research

journal homepage: www.elsevier.com/locate/csr

Coherence between infragravity waves and ambient water motions over cape-associated shoals

Juan F. Paniagua-Arroyave[a,b,c,*], Arnoldo Valle-Levinson[d], Peter N. Adams[a], Sabrina M. Parra[d,e]

[a] Department of Geological Sciences, University of Florida, Gainesville, FL, USA
[b] Área de Ciencias del Mar, Departamento de Ciencias de la Tierra, Universidad EAFIT, Medellín, Antioquia, Colombia
[c] Department of Earth, Ocean, and Atmospheric Science, Florida State University, Tallahassee, FL, USA
[d] Department of Civil and Coastal Engineering, University of Florida, Gainesville, FL, USA
[e] American Society for Engineering Education Postdoctoral Fellow at the Naval Research Laboratory, Stennis Space Center, MS, USA

ARTICLE INFO

Keywords:
Cross-shelf exchange
Infragravity waves
Tides
Subtidal motions
Florida Current
Cape-related shoals
Cape Canaveral
Coherence analysis

ABSTRACT

Cross-shelf water motions influence fluxes of nutrients, larvae and sediments, which in turn affect nearshore morphodynamics. Among these motions are infragravity waves, which typically exhibit periodicities from 20 to 200 s, and originate from multiple sources including the superposition of incident wave fields. To examine how infragravity waves co-vary with water motions in an area of complex bathymetry, we analyzed measurements from acoustic Doppler current profilers around cape-associated shoals near Cape Canaveral, on the Florida (USA) Atlantic coast. Observations of water motions and infragravity wave heights at the outer and inner swales of two isolated shoals (Shoal E and Shoal D), located approximately 15 km offshore in ~ 14 m water depth, were subjected to squared coherency and wavelet coherence analyses. Coherences between infragravity wave heights and flow conditions were unsteady, i.e. variable over time, and exhibited differences between outer and inner swales. Subtidal flows (periods > 0.5 days) were sporadically coherent with the total and bound infragravity wave heights at both inner and outer swales. Tidal flows (~ 2 cycles/day) were coherent with the total infragravity wave heights only at outer swale locations. These results indicate that tidal motions may modulate the generation of free (directed both oppositely to and in the direction of short-wave propagation) infragravity waves by short-wave groups shoaling and by refractive trapping at shoals. Subtidal flows, on the other hand, may influence triad interactions that generate infragravity motions.

1. Introduction

Cross-shelf exchanges of material are controlled by relatively weak, yet relevant flows that dictate the fate of larvae, pollutants, and sediments (Nittrouer and Wright, 1994; Brink, 2016). At cape-related inner shelves, sediment fluxes are actually driven by combinations of bathymetry-controlled water motions of different periods. These processes include tidal rectifications, wind-driven currents, resuspension by wave-orbital velocities, and longshore drift gradients (Geyer, 1993; McNinch and Luettich, 2000; Kumar et al., 2013; Limber et al., 2017, and others).

Also known as headland-associated linear sandbanks (Dyer and Huntley, 1999), cape-related shoals have been shown to migrate up to 10 m/yr (Olsen Associates, 2013; Thieler et al., 2014), supporting the idea that they have been reworked by oceanographic processes during the Holocene (Field and Duane, 1974; McNinch and Luettich, 2000). Shoals ultimately act as sediment sinks because wave-related longshore currents lose transport capacity at the cape tip (Limber et al., 2017) and offshore-directed, tidal-residual flows relocate sediment seaward, away from the headland (Signell and Geyer, 1990; Geyer, 1993; Berthot and Pattiaratchi, 2006, and others). Cross-shelf exchanges of material off capes are therefore governed by flow separation of wind-driven currents (Kumar et al., 2013; Lamas et al., 2017) and the well-known Ekman transport (Pedlosky, 1987, Section 4.3). Over cape-related shoals, cross-shelf exchange may also be influenced by short-wave-related motions (Lentz et al., 2008), and infragravity waves (Thomson et al., 2005; Pomeroy et al., 2012; Winter et al., 2017).

Long gravity waves (LGWs, also known as infragravity waves) have been found to exert a first order control on nearshore morphodynamics (Bertin et al., 2018, and references therein). Under non-breaking conditions, irrotational LGWs (typically from 5 to 50 mHz, or 20 to 200 s) propagate either as oscillations bound to short-wave groups (Longuet-

* Correspondence to: Juan Felipe Paniagua Arroyave, Departamento de Ciencias de la Tierra, Universidad EAFIT, Carrera 49 # 7 Sur - 50, Oficina 19-613, Colombia.
E-mail address: jpaniag2@eafit.edu.co (J.F. Paniagua-Arroyave).

https://doi.org/10.1016/j.csr.2018.12.003
Received 2 April 2018; Received in revised form 29 September 2018; Accepted 4 December 2018
Available online 11 December 2018
0278-4343/

Higgins and Stewart, 1962; Herbers et al., 1994), nearshore-trapped edge waves (Lippmann et al., 1999; Sheremet et al., 2005; Winter et al., 2017), or free waves (Herbers et al., 1995). Both forced and free infragravity motions have been found to contribute to nearshore sand fluxes, especially during storms (Ruessink et al., 1998; Aagaard and Greenwood, 2008; de Bakker et al., 2016a). Although LGW contributions to the cross-shelf material transport over cape-related shoals are not well understood, it is likely that they generate both onshore- and offshore-directed transport. Infragravity wave variability over cape shoals might also be related to partial reflections and trapping (Herbers et al., 1995; Rijnsdorp et al., 2015; Zou, 2011), and add to other phenomena that can influence the effect waves exert on ambient currents (Lane et al., 2007).

The objective of this study is to explore the relationship between LGWs and ambient flows at cape-related shoals. This exploration is done mainly with coherence and wavelet coherence analyses of velocity and water level data collected off Cape Canaveral, Florida, USA. In Section 2 we describe the study area, the data collection schemes, and the data analysis. We compare LGW heights to flow conditions, particularly water depth, principal-, and secondary-axis velocities. Section 3 presents the main findings revealed by these comparisons. Coherence between LGW motions and flow conditions were found to be variable over time and spatially heterogeneous (different in outer and inner swales of isolated shoals). The focus of Section 4 is to explain tidal and subtidal coherences found in Section 3 and to provide additional evidence of the coherence between LGWs and synoptic phenomena, i.e. the Florida Current transport and wind speed. We do not, however, claim that these processes produce the observed infragravity motions, because short-gravity wave variability appears to explain the majority of LGW energy, as expected. We, instead, suggest that winds and geostrophic flows modulate the water level that influences LGW variability over the relatively shallow bathymetry of cape-related shoals. Conclusions are in Section 5.

2. Data and methods

2.1. Cape Canaveral shoals

Cape Canaveral shoals are found surrounded by depths between 5 and 25 m offshore of the Cape Canaveral region, on the Atlantic coast of central Florida. Shore-attached Southeast shoal and Chester shoal appear as offshore extensions of Cape Canaveral and False Cape, respectively. This study concentrates on Shoal E and Shoal D (Fig. 1), which are separated by ~ 5 km from Southeast and Chester shoals (Field and Duane, 1974; Thompson et al., 2015). Observations were conducted on the inner and outer swales of Shoal E, and on both swales plus the ridge of Shoal D. Inner locations, therefore, refer to the inner swales of Shoal E and Shoal D during all deployments. In the Fall 2015 deployment, however, inner location refers to Shoal D ridge. Instruments were not moored simultaneously at all locations, which prevented data comparison among sites. However, we assume data can be comparable when considering that they represent cape-related shoal hydrodynamics over a range of conditions.

Offshore wave characteristics, ~ 25 km from the observations over shoals, were obtained from the National Oceanic and Atmospheric Administration's (NOAA) National Data Buoy Center (NDBC) buoy 41009 (Fig. 2). During all deployments, waves commonly exhibited peak periods, T_p, ~ 8 ± 2 s (Fig. 2 F–J) and approached from directions between East and East-North-East (i.e. $D_p = 60 - 90$ °T) (Fig. 2 K–O). Significant wave heights, the mean of the highest one-third waves, H_s, were typically less than 1.5 m, but exceeded 2.5 m during energetic conditions. Winds had maximum speeds >8 m/s and exhibited diurnal (sea breeze) periodicities (Fig. 2 A–E). While wind variability at buoy 41009 may not represent the conditions at Canaveral shoals, it was the closest oceanic record available. Wind measurements closer to the sampling site are required (Kumar et al., 2013).

2.2. Data analysis

2.2.1. Field measurements

Water velocity profiles and near-bottom pressure were measured near Shoal E and Shoal D (Fig. 1 D and E) during five deployments from Fall 2013 through Fall 2015, with 3 deployments at Shoal E and 2 at Shoal D. Two data collection schemes were used. Water depth, h, and profiles of velocity, $\bar{q}(z)=(u, v)$ (with u and v as the east-west and north-south velocity components, respectively, and z the vertical distance), were measured as ensembles per fraction of 1 h (typically 3 min). Values of $\bar{q}$ were measured between 1 m above the instrument and ~ 90% of total water depth due to side-lobe effects at 0.5 m cells. This scenario is referred to as *currents*. In addition, pressure and velocity ~ 2 m below the surface were recorded at 2 *Hz* either continuously or in bursts of 1200, 2048, and 3600 data per hour (or fraction of *hour*) adjusted for each instrument's functionality and battery availability. The total amount of data per burst limited the statistical reliability acquired by windowing. Minimum frequency (or maximum period) resolved by the Fourier transformation depended on length of windows as explained later. This second scheme was used to examine *waves*.

Velocities collected using the currents scheme were rotated by an angle θ_p that matched the principal-axis of the flow, which is (Thomson and Emery, 2014, Eq. 4.52b)

$$\theta_p = 0.5 \arctan\left[\frac{2\langle u'v'\rangle}{\langle u'^2\rangle - \langle v'^2\rangle}\right], \quad (1)$$

where u' and v' represent the demeaned time series of east and north velocity components, and $\langle\ \rangle$ indicates averaging in time. Depth-averaged velocities were then calculated from the principal-, U, and secondary-axis, V, velocities as (e.g. for U) $\overline{U} = 1/(z_s - z_b)\int_{z_b}^{z_s} U(z)dz$, where z_s and z_b are the distances to the surface and bottom velocity measurements, respectively. See Paniagua-Arroyave et al. (2018) for details of the deployment set-up and data analysis.

2.2.2. Spectrograms and band-specific significant wave heights

A power spectrum was quantified for each 1-h package of detrended and attenuation-corrected bursts of pressure from the *waves* sampling scheme. Each package was block-averaged and Fourier transformed using segments of Hanning windows of 2^9 (windows of 256 s) elements overlapped by 75%. For each spectrum, significant wave heights were quantified for the infragravity and short-gravity wave (SGW) frequency bands as, e.g. for LGWs, $H_{LGW} \approx 4\sqrt{m_{LGW}}$ (Holthuijsen, 2007, Eq. 4.2.24 therein), where $m_{LGW} = \int_{f_{min}}^{50\ mHz} df\ S(f)$ is the zeroth-moment of the sea surface variance spectrum for the infragravity band, and $f_{min} = 1/256$ s = 3.9 mHz (Thomson and Emery, 2014, their Eqs. 5.121 and 5.6.3). Oscillations at frequencies between 50 and 300 mHz (periods from ~ 3 to 20 s) were considered to be the SGWs.

Fig. 3 shows the spectrograms, $\mathcal{S}(t, f)$, and the SGW significant wave heights, H_{SGW}, for each deployment. Spectrograms represent the time series of variances at all frequencies resolved by our methodology, whereas H_{SGW} corresponds to the mean value of the highest one-third of waves measured in the range between 3 and 20 s. These values are presented for each deployment at inner and outer locations. Variances at LGW frequencies (nominally between 5 and 50 mHz, or 20–200 s) covary with H_{SGW}, especially for SGW waves larger than ~ 1.5 m (Fig. 3 A–J).

2.2.3. Coherence between LGW heights and water motions

The LGW tidal and subtidal variabilities, however, are not obvious from a visual inspection of the spectrograms. Application of coherency squared calculations allowed confirmation of this co-variability at periods ranging from 0.25 to 16 days (or 4 to ~ 0.06 cycles/day), of water level and velocity (from the currents scheme) with LGW heights. To analyze the average co-

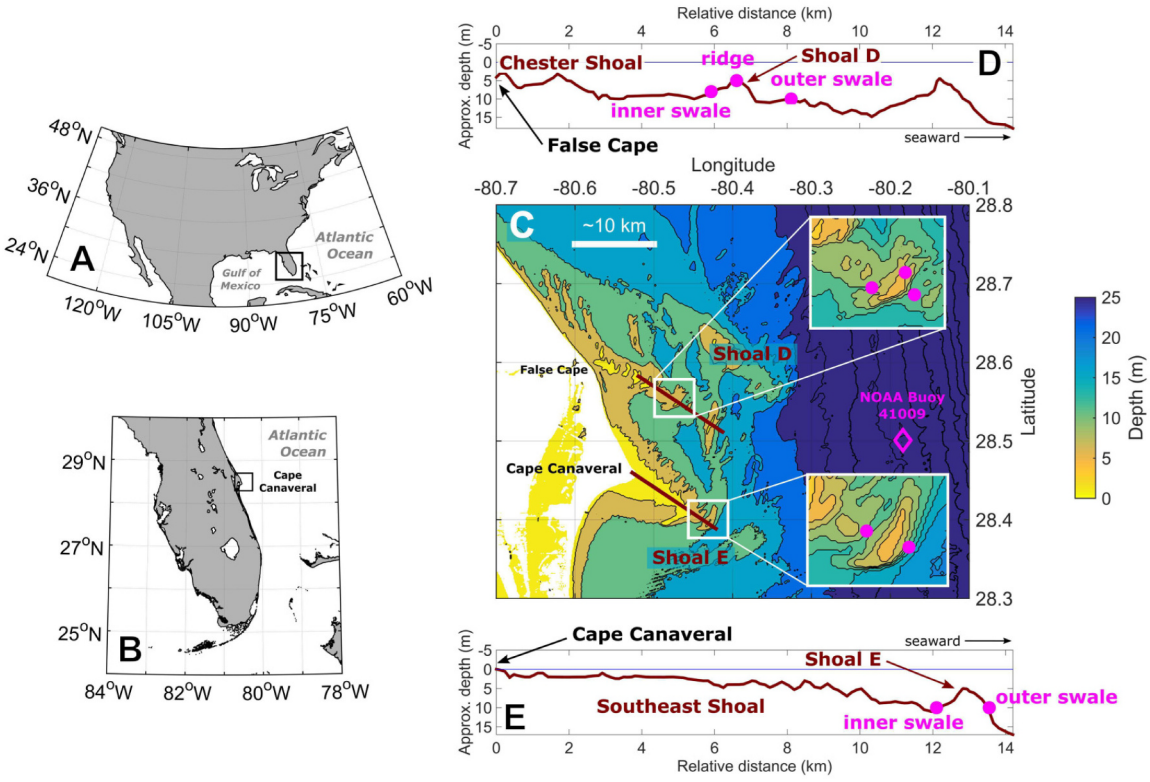

Fig. 1. Cape Canaveral shoals and mooring locations of acoustic Doppler current profilers (ADCPs). Magenta filled circles indicate ADCP locations near Shoal D and Shoal E. The magenta diamond shows the location of the NOAA buoy 41009. Black rectangles in A and B show the location of Florida Peninsula (within North America) and Cape Canaveral on the Florida Peninsula, respectively. The map in C shows the bathymetry near Cape Canaveral with an inset highlighting shoals E and D. Contours indicate water depths at intervals of 5 m. Brown line corresponds to bottom depths across Chester Shoal and Shoal D (D) and Southeast shoal and Shoal E (E). The bathymetric data were obtained from NOAA through its Geophysical Data Repository (resolution of 3 arc-seconds of longitude and latitude). The package M_Map was used to create North America and Florida maps (https://www.eoas.ubc.ca/rich/map.html). (For interpretation of the references to colour in this figure legend, the reader is referred to the web version of this article.)

variability between LGW waves and water motions, squared coherence spectra –squared coherencies–, $\gamma^2_{(x,\log_{10}[H_{LGW}])}$, were calculated for base-10 logarithms of H_{LGW} (Jenkins and Priestley, 1957, their Section 7) given that H_{LGW} time series were typically non-stationary (Dickey and Fuller, 1979), and parameters measured using the currents scheme (water level and velocity components) as

$$\gamma^2_{(x,\log_{10}[H_{LGW}])} = \frac{|\mathcal{S}_{(x,\log_{10}[H_{LGW}])}|^2}{\mathcal{S}_x \mathcal{S}_{\log_{10}[H_{LGW}]}}, \tag{2}$$

where $\mathcal{S}_{(x,\log_{10}[H_{LGW}])}$ represents the cross-spectral density between time series x and $\log_{10}[H_{LGW}]$ (with x representing h, $\overline{U}$, and $\overline{V}$) for a given frequency (Thomson and Emery, 2014, their Section 5.6.6). In such case, $\mathcal{S}_{\log_{10}[H_{LGW}]}$ is the power spectral density (or autospectrum) of time series $\log_{10}[H_{LGW}]$ for a frequency. Statistically significant squared coherency values were calculated as (Thomson and Emery, 2014, their Eq. 5.173)

$$\gamma^2_{1-\alpha} = 1 - \alpha^{[1/(EDof-1)]}, \tag{3}$$

where $EDof$ represents the number of independent values used to smooth the cross-spectra in each frequency band in some cases multiplied by a factor, i.e. 8/3 for Hanning windows (Thomson and Emery, 2014, their Table 5.5), and α is given by the confidence interval, e.g. for 95% $\alpha = 0.05$. The phase (in °) between x and H_{LGW} is given by

$$\phi_{(x,\log_{10}[H_{LGW}])} = \arctan\left\{\frac{\Im[\mathcal{S}_{(x,\log_{10}[H_{LGW}])}]}{\Re[\mathcal{S}_{(x,\log_{10}[H_{LGW}])}]}\right\} \times \frac{180°}{\pi}, \tag{4}$$

with $\Im[\mathcal{S}_{(x,\log_{10}[H_{LGW}])}]$ and $\Re[\mathcal{S}_{(x,\log_{10}[H_{LGW}])}]$ representing cross-spectrum imaginary and real arguments, respectively. Depending on the frequency under consideration, f, phases represent the temporal lag between time series x and $\log_{10}[H_{LGW}]$. A phase of 0°, for example, represents both time series modulating together. Similarly, $\phi_{(x,\log_{10}[H_{LGW}])}$ equal to − 90° indicates x leading $\log_{10}[H_{LGW}]$ (90° suggests $\log_{10}[H_{LGW}]$ leading x) by a time lag equal to $\phi_{(x,\log_{10}[H_{LGW}])}/(360°f)$. Coherence spectra were smoothed over consecutive frequency values using Hanning windows of 16 elements, except for outer locations during Spring and Fall of 2015 for which 8 elements were used given that time series were shorter.

Coherency analysis was expanded to include variations in the time and frequency domains. The time series of wavelet coherence values between x and H_{LGW}, $WTC_{(x,H_{LGW})}$, were then calculated for each scale, s, following (see Appendix in Torrence and Webster, 1999)

$$WTC_{(x,H_{LGW})} = \frac{|\langle s^{-1} W_{(x,H_{LGW})}\rangle|^2}{\langle s^{-1}|W_x|^2\rangle\langle s^{-1}|W_{H_{LGW}}|^2\rangle}, \tag{5}$$

where W_x and $W_{H_{LGW}}$ are the wavelet transforms of x and H_{LGW}, respectively (Torrence and Compo, 1998, their Eq. 4), $W_{(x,H_{LGW})}$ is the cross-wavelet spectrum, s is the scale (a measure of period), and $\langle\ \rangle$ represents smoothing in time and scale. The phase (per scale) between time series x and H_{LGW}, $\Phi_{(x,H_{LGW})}$, was obtained from

$$\Phi_{(x,H_{LGW})} = \arctan\left\{\frac{\Im[\langle s^{-1} W_{(x,H_{LGW})}\rangle]}{\Re[\langle s^{-1} W_{(x,H_{LGW})}\rangle]}\right\} \times \frac{180°}{\pi}, \tag{6}$$

which comes from the same principle as Eq. (4). Statistical confidence intervals for $WTC_{(x,H_{LGW})}$ values were calculated by means of Monte Carlo simulations of synthetic signals with spectral characteristics similar to those of the time series analyzed (Grinsted et al., 2004, their Section 3.4).

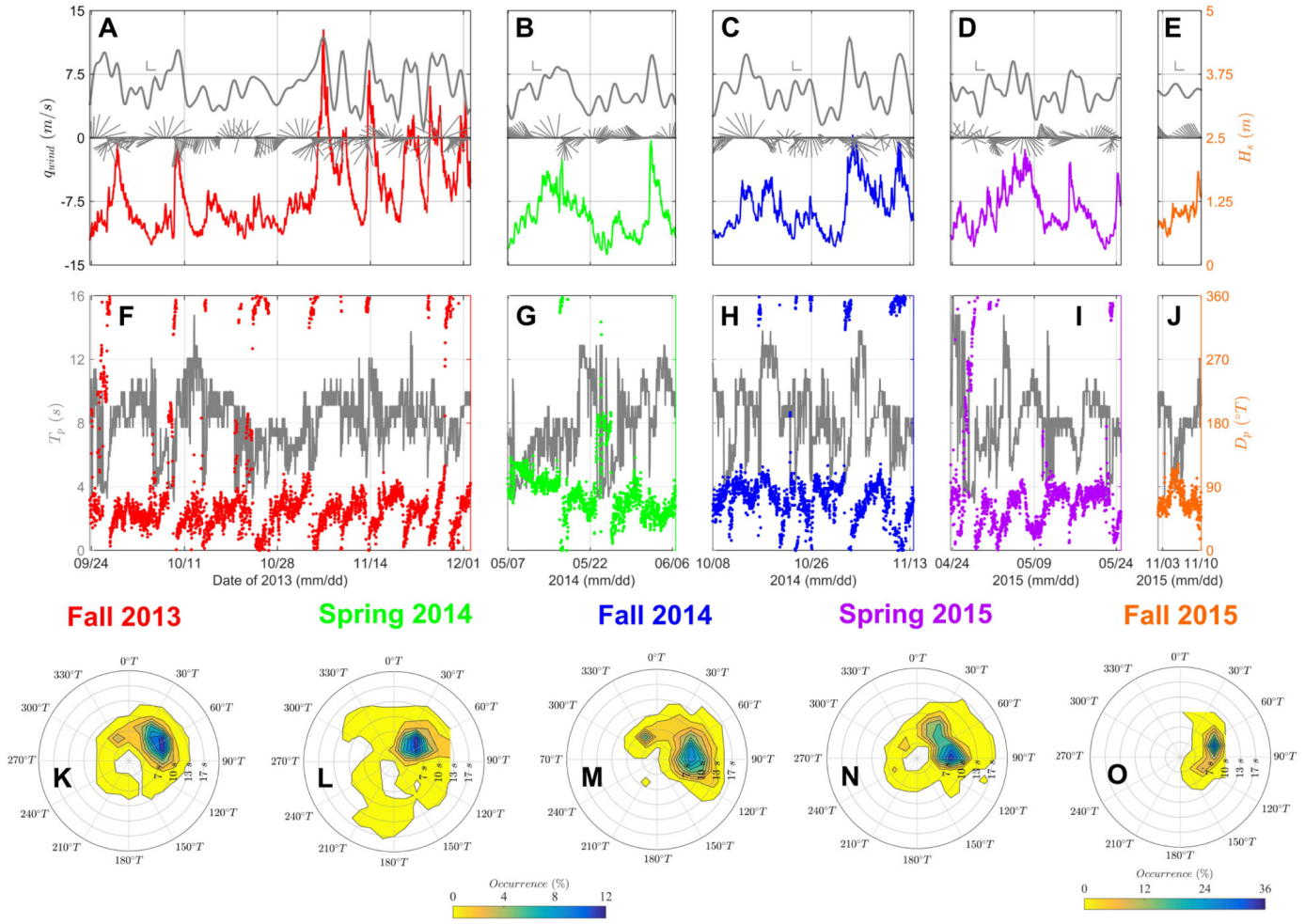

Fig. 2. (A–J) Wave statistics at the NOAA buoy 41009 (28.501N, 80.184W, 40-m deep) offshore of Cape Canaveral, Florida Atlantic coast, during each deployment. (A–E) Colored lines indicate the significant wave heights, H_s, while gray lines show the wind speeds, q_{wind} in m/s, with gray sticks pointing to the direction of wind origin. (F–J) Gray lines show the peak period, T_p (in s) while colored dots show the peak direction, D_p (in °T). (K–O) Polar joint histograms of peak direction, D_p, and peak period, T_p (in s). Contours indicate the percentage of occurrence of a combination of period and direction. K–N are represented by the first colorbar (0–12%) and O is represented by the second colorbar (0–36%). Buoy data were obtained from the NOAA National Data Buoy Center (NDBC) at http://www.ndbc.noaa.gov/station_page.php?station=41009/. (For interpretation of the references to colour in this figure legend, the reader is referred to the web version of this article.)

3. Results

3.1. Coherence between water levels and LGWs

Fig. 4 shows the coherency squared per frequency (in cycles/day) between h and H_{LGW} measured during each deployment and at each location. Water level variations were coherent with H_{LGW} at tidal frequencies –approximately 2 cycles/day– at all outer locations (Fig. 4B). Phases related to these coherences were ~ 0° (no temporal lag) for Spring and Fall 2014, – 45° (h leading H_{LGW} by ~ 1.5 h) for Spring and Fall 2015, and 90° (H_{LGW} leading h by ~ 3 h) for Fall 2013 (Fig. 4D). Only during Spring 2015, however, h and H_{LGW} were highly coherent ($\gamma^2 > 0.75$) at the inner swale of Shoal D, with ϕ close to 45°, or H_{LGW} leading by 1.5 h (Fig. 4 A and C).

Subtidal coherencies between h and H_{LGW}, those at frequencies <0.5 cycles per day, were found for observations from Fall 2013 at both locations (Fig. 4A and B). Phases were close to zero. There was also high coherence at over-tidal frequencies, ~ 4 cycles/day, at the outer swale of Shoal D during Spring 2015 (Fig. 4B) with ϕ values ~ 90° (H_{LGW} leading h by 1.5 *hours*) (Fig. 4 C and D).

Fig. 5 shows, for each deployment, time series of water depth and infragravity wave heights, along with their wavelet coherence spectra and phases. Unsteady, yet high coherences (WTC> 0.75) were found at periods ~ 0.5 and ~ 8 days for some of the deployments. These high coherences were exhibited during all deployments at the outer locations (bottom panels in Fig. 5 B, D, F, H, and J), and during Fall 2014 and Spring 2015 at the inner sites (bottom panels in Fig. 5 E and G). Note that the temporal scales for inner and outer locations differ in Fig. 5.

Phases that remain relatively constant throughout periods of significant coherence indicate reliable phase behavior, which suggests that time series were connected by a physical mechanism. However, phases varied with deployments and measurement location. During Fall 2013 at the outer swale of Shoal E phases were ~ 90° at 0.5 days (H_{LGW} leading h by 3 h) and ~ 0° at 3 days (no lag). Phases were ~ 45° at 8 days (H_{LGW} leading h by 1 day) for both locations (bottom panels in Fig. 5 A and B). During Spring 2014 (Fig. 5 D) and Fall 2014 (Fig. 5 F) at the outer swale of Shoal E, phases were approximately − 45° at 0.5 days (h leading H_{LGW} by 1.5 h), and ~ –90° at 8 days (h leading H_{LGW} by 48 h). During Fall 2014, h and H_{LGW} were not coherent at subtidal frequencies. During Spring and Fall 2015 at the ridge (Fig. 5 H) and outer swale (Fig. 5 J) of Shoal D, phases at 0.5 days were ~ –45° (h leading H_{LGW} by 1.5 h). At 8 days, phases were ~ 90° (H_{LGW} leading h

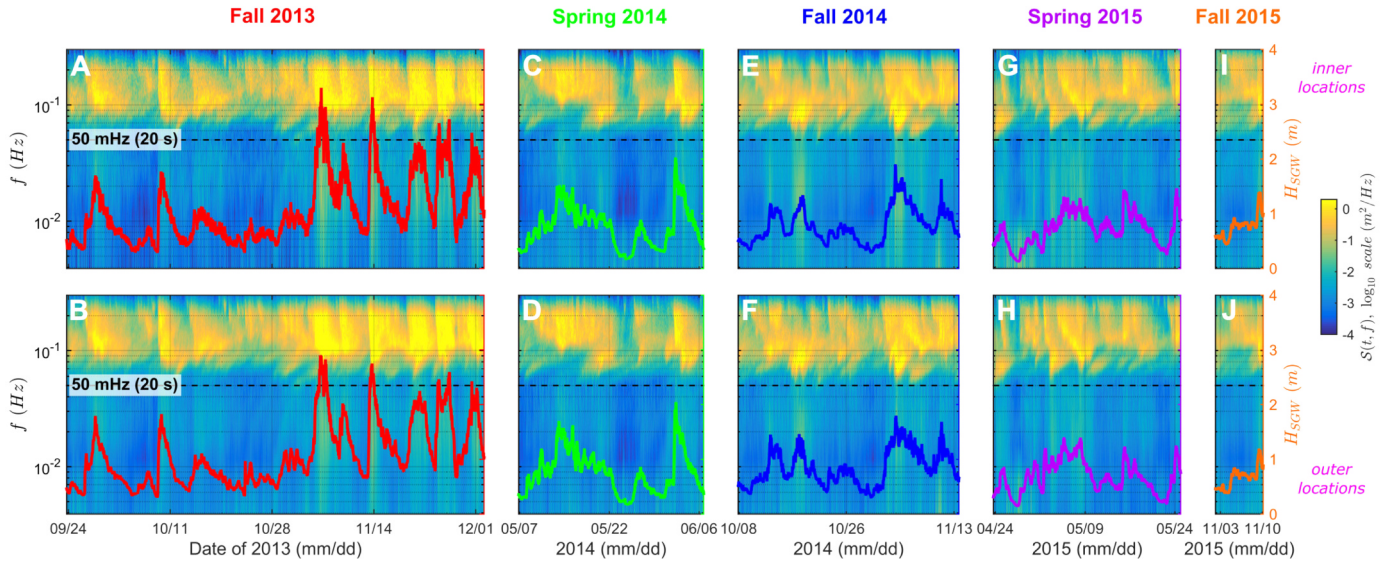

Fig. 3. (A–J) Spectrograms –time series of spectra– and SGW significant wave heights during each deployment at each location. Values in colormaps correspond to the variance at each frequency (left vertical axes) at a particular time, with the right colorbar indicating that value in logarithmic scale. Values of short-wave heights, S_{SGW}, correspond to right axes in all panels. Dashed lines indicate the limit at 50 mHz (or 20 s) that separate short-waves from infragravity motions. For comparison purposes, the time limit in each panel was chosen to match the time span when both inner and outer locations were deployed concurrently. (For interpretation of the references to colour in this figure legend, the reader is referred to the web version of this article.)

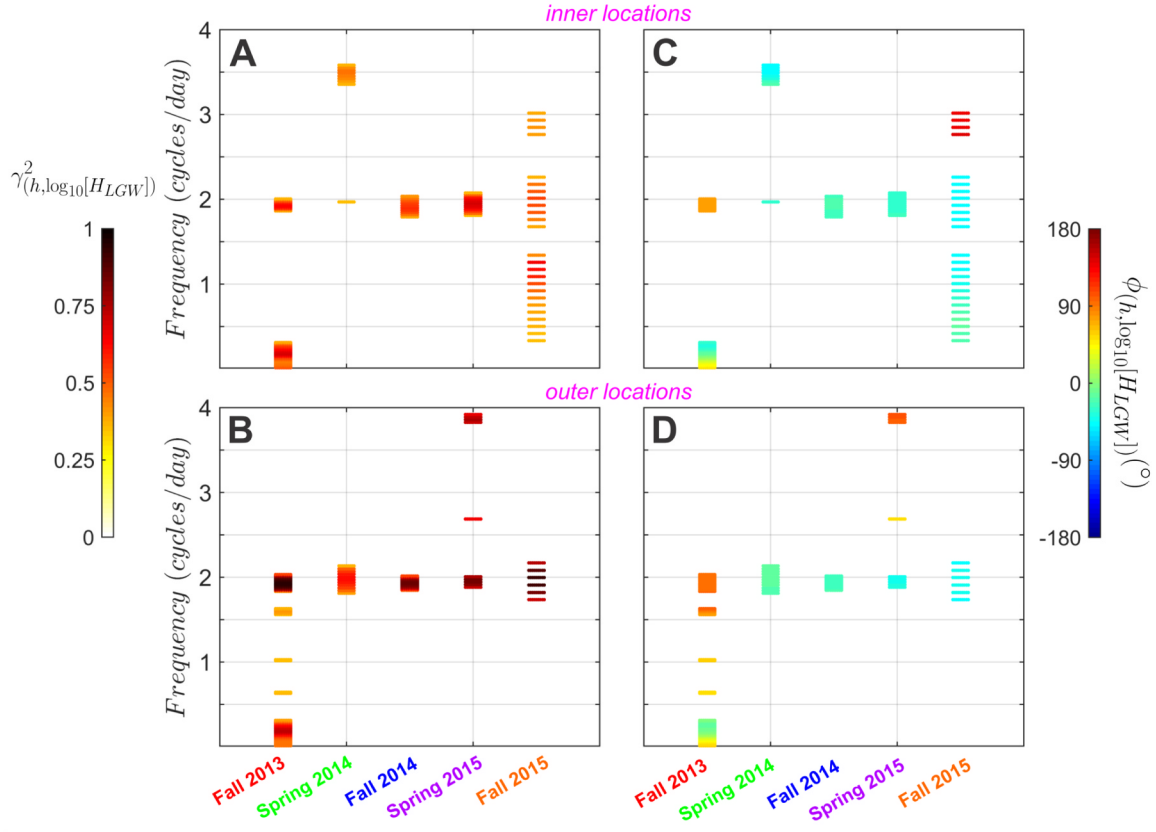

Fig. 4. Scatter plots showing coherence spectra and phases between h and $\log_{10}[H_{LGW}]$ at each site for all deployments. Left panels (A and B) show the statistically significant (95%) values of squared coherency, $\gamma^2_{(h,\log_{10}[H_{LGW}])}$, whereas right panels (C and D) display the phase, $\phi_{(h,\log_{10}[H_{LGW}])}$. Cross-spectral values from inner locations were smoothed using segments of 2^4 elements (i.e., $EDof = 8/3 \times 2^4 = 42.\ \bar{6}$). For outer locations $EDof$ values were $8/3 \times 2^4 = 42.\ \bar{6}$ for Fall 2013, Spring 2014, and Fall 2014; while $EDof = 8/3 \times 2^3 = 21.\ \bar{3}$ for Spring 2015 and Fall 2015. Vertical axes correspond to frequency in cycles/day. Coherence and phase values correspond to left and right colorbars, respectively. Upper panels show results for the inner locations, whereas lower panels represent outer sites. (For interpretation of the references to colour in this figure legend, the reader is referred to the web version of this article.)

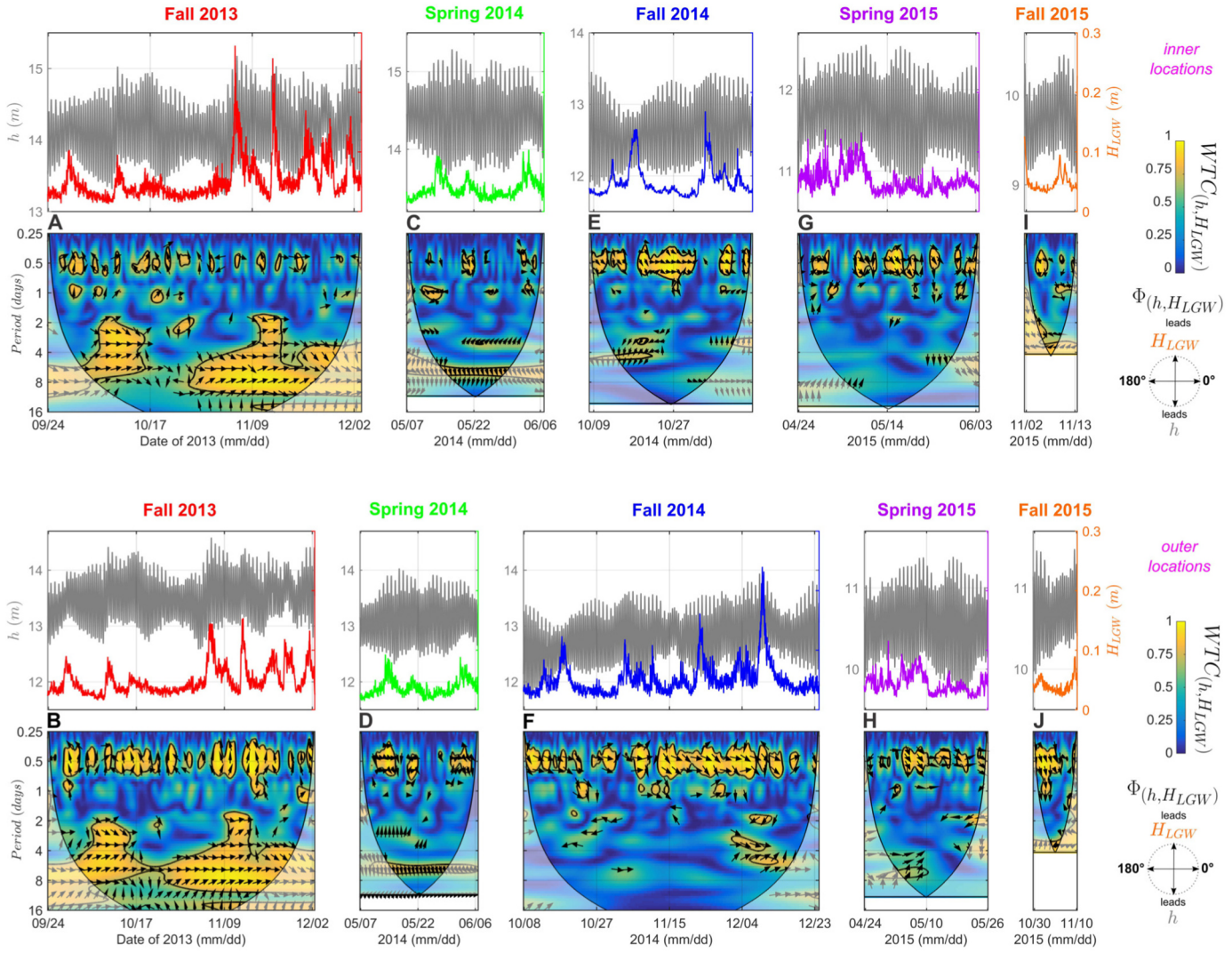

Fig. 5. Time series of h (gray) and H_{LGW} (color), and their wavelet coherence spectra and phases, $WTC_{(h,H_{LGW})}$ and $\Phi_{(h,H_{LGW})}$, for each deployment and site. Each subplot (e.g., A) is formed by panel pairs consisting of time series and wavelet coherence spectra. Upper and lower rows of subplots (e.g., A, C, E, G, and I) represent the calculations at a location. Wavelet coherence plots show levels of coherency at a period and time. Black lines enclose portions of statistically significant coherence at the 95% level of confidence. Right-angle of arrows represent the phase between time series, with h as the first time series used in calculation (see legend in the lower right part of each subplot collection). Shaded regions (cone of influence) indicate where edge effects become important and coherence estimates are not reliable. (For interpretation of the references to colour in this figure legend, the reader is referred to the web version of this article.)

by 48 h) with moderate coherence (~ 0.5) at the ridge. These 8-day oscillations in H_{LGW} were not within the period scope during the Fall 2015 deployment.

3.2. Coherence between $\overline{U}$ and LGWs

Fig. 6 shows the squared coherence between $\overline{U}$ and H_{LGW}. These time series were highly coherent (γ^2> 0.75) at ~ 2 cycles/day at the outer locations during Fall 2013, Spring 2015 and Fall 2015. Time series were moderately coherent during Spring and Fall 2014 (Fig. 6 B). At the inner sites, in contrast, the time series were highly coherent only during Spring 2015, and moderately coherent ($\gamma^2\approx$ 0.50) during Spring 2014 and Fall 2015 (Fig. 6 A). At the outer location, phases at ~ 2 cycles/day were ~ 45° (H_{LGW} leading by 1.5 h) during Spring 2014; ~ 0° (no lag) during Fall 2014; and ~ 135° (H_{LGW} leading by 4.5 h) during Fall 2013, Spring and Fall 2015 (Fig. 6D). At the inner locations, phases were ~ 135° (H_{LGW} leading by 4.5 h) during Fall 2013, ~ 0° (no lag) during Spring 2014, ~ − 90° (h leading by 3 h) during Spring 2015, and ~ 90° (H_{LGW} leading by 3 h) during Fall 2015 (Fig. 6C).

Infragravity wave heights and depth-averaged principal-axis velocities were moderately coherent ($\gamma^2\approx$ 0.50) at subtidal frequencies during Fall 2013 at both inner and outer locations. Phases were approximately 135° (Fig. 6 A–C). Those values suggest that the increase in H_{LGW} preceded the peak in principal-axis velocities by 18 h at a frequency of 0.5 cycles/day.

Temporal variability in coherences (bottom panels in all subplots of Fig. 7) suggests $\overline{U}$ co-varied with H_{LGW} at tidal periods during some instances. Phase values, however, were not consistent at periods ~ 0.5 days (~ 2 cycles/day). At subtidal periods of ~ 8 days, phases indicated consistency during Fall 2013, Fall 2014, and Spring 2015 at the corresponding inner and outer locations (bottom panels in Fig. 7A, B, E–H). These phases indicate H_{LGW} preceded $\overline{U}$ by a time lag of 2 (90°) to 3 (135°) days.

3.3. Coherence between $\overline{V}$ and LGWs

Fig. 8 shows the squared-coherency spectra between $\overline{V}$ and H_{LGW}. At tidal frequencies, they were highly coherent (γ^2> 0.75) at the outer location during all deployments, except for Spring 2014 when $\gamma^2\approx$ 0.5. This high coherence was observed at an inner location during only one

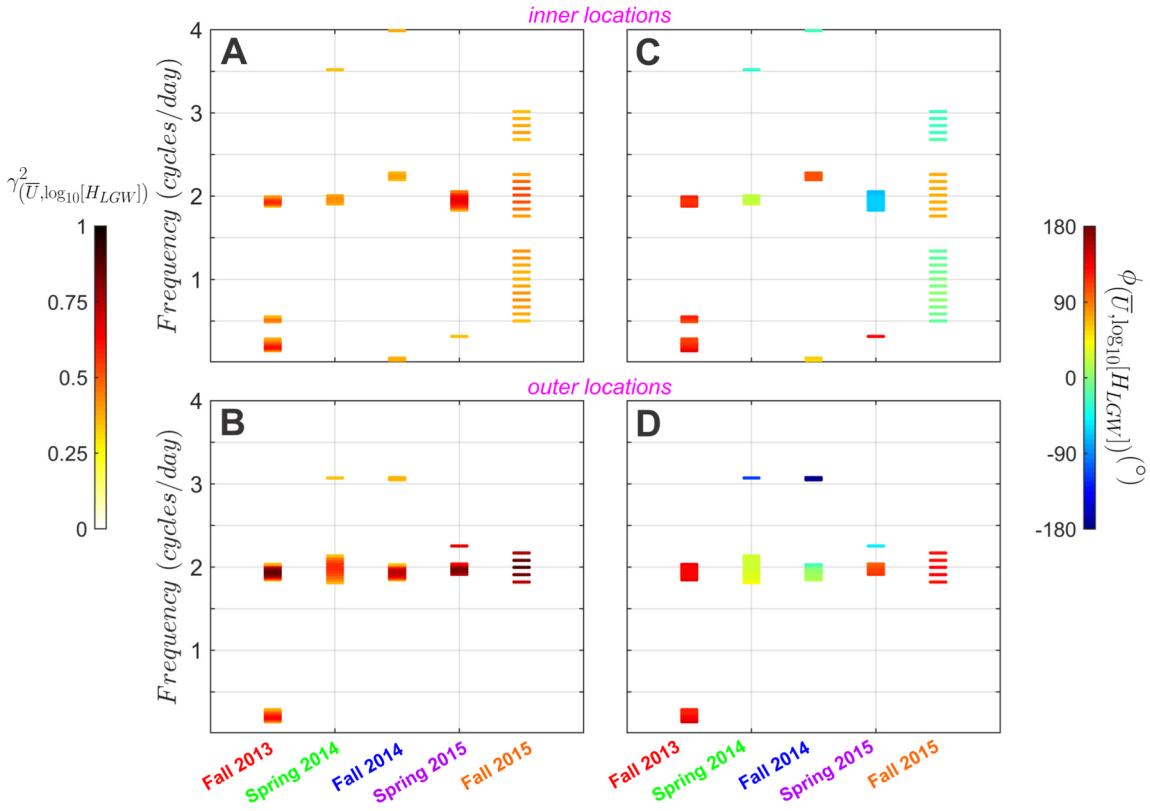

Fig. 6. Scatter plot showing coherence spectra and phases between $\overline{U}$ and $\log_{10}[H_{LGW}]$ at each site of all deployments. The same formatting as Fig. 4 is used.

deployment (Spring 2015). Phases for deployments of high coherence at outer locations were approximately 0° (no lag) for Fall 2013, − 90° ($\overline{V}$ leading by 3 h) for Spring 2014, − 180° ($\overline{V}$ leading by 6 h) for Fall 2014, and 45° (H_{LGW} leading by 1.5 h) for Spring and Fall 2015 (Fig. 8D). High coherences at subtidal periodicities (frequencies less than 0.5 cycles/day) were found during Spring and Fall 2015, with ϕ approximately equal to − 180 and − 45° ($\overline{V}$ leading by 6 and 1.5 h), respectively.

Fig. 9 shows, for each location and deployment, the time series of $\overline{V}$ and H_{LGW} along with their wavelet coherence spectra. Physically consistent coherency at ~ 0.5 days, i.e. instances exhibiting statistically significant wavelet coherence and nearly constant phases, was observed during some instances at all outer locations (bottom panels in Fig. 9 B, D, F, H, and J). Values of $\Phi_{(\overline{V},H_{LGW})}$ varied notably: 0° (no lag), − 90° ($\overline{V}$ leading by 3 h), − 135° ($\overline{V}$ leading by 4.5 h), 45° (H_{LGW} leading by 1.5 h), and 90° (H_{LGW} leading by 3 h) for Fall 2013, Spring 2014, Fall 2014, Spring 2015, and Fall 2015, respectively. At the inner location during Spring 2015 (bottom panel in Fig. 9G) coherences were consistent, although unsteady, during the deployment. Phases were ~ − 135° ($\overline{V}$ leading by 4.5 h) in this case. Subtidal $\overline{V}$ motions at the inner locations were coherent with H_{LGW} during certain periods of Fall 2013 and 2014, with $\Phi_{(\overline{V},H_{LGW})} \approx -45$ and 90° ($\overline{V}$ leading by 1.5 h and H_{LGW} leading by 3 h), respectively.

4. Discussion

Differences in coherence between ambient flows and H_{LGW} suggest that infragravity wave variability was modulated by processes with time scales and locations within the shoals. Tidal and subtidal flows have been found to be affected by cuspate forelands and related inner-shelf bathymetry (Geyer, 1993; McNinch and Luettich, 2000; Lamas et al., 2017). These flows may exert control on cross-shelf exchange, among other processes, by influencing infragravity wave variability. We consider the influence of tidal and subtidal motions on LGWs separately given the observed spatial differences in coherences. Possible influences include offshore-onshore migrations in the turning point of shoal- and shoreline-reflected LGWs (Eckart, 1951; Huntley et al., 1986; Rijnsdorp et al., 2015), variability in water depth and bathymetric profile shape (Sand, 1982; Thomson et al., 2006; de Bakker et al., 2016b), and interactions between short-wave groups and horizontally sheared subtidal velocities (Liu et al., 1990). In particular, we envision shoal-trapping of edge waves, which is modulated by ambient motions, to exert control on the maintenance of isolate shoals. Such a mechanism would operate at Shoal D and Shoal E in analogy to bar-trapping at alongshore-uniform bars (Bryan and Bowen, 1996; Rijnsdorp et al., 2015).

4.1. Tidal variability of LGWs over cape-related shoals

Spatial variability in coherence at tidal frequencies suggests that cape shoals might influence the tidal modulation of LGWs. Tidal modulations of infragravity waves have been found by previous studies in the surfzone (Thomson et al., 2006) and inner shelves 8–30 m deep (Okihiro and Guza, 1995). In the shoaling and surf zones, this modulation is considered to occur because the nearshore bathymetry (i.e. the overall profile shape) varies according to tidal stage, thereby controlling nonlinear interactions between sea-swell and infragravity motions. During low tide, nonlinear energy transfers from LGWs to SGWs are enhanced, decreasing the amplitude of infragravity oscillations. The outgoing LGWs are therefore reflected from the shoreline with amplitudes that are smaller than their counterparts during high tide (Thomson et al., 2006). The tidally modulated reflected LGWs actually provide an explanation for the tidal variability of LGWs observed at inner shelves in ~ 20 m water depth (Okihiro and Guza, 1995). The tidal modulation is explained by the fact that total energy transfers depend upon the horizontal extent of SGW propagation. As found by Thomson et al. (2006), energy transfers from short to long waves are smaller over a convex, low-tide profile for a constant tidally-averaged

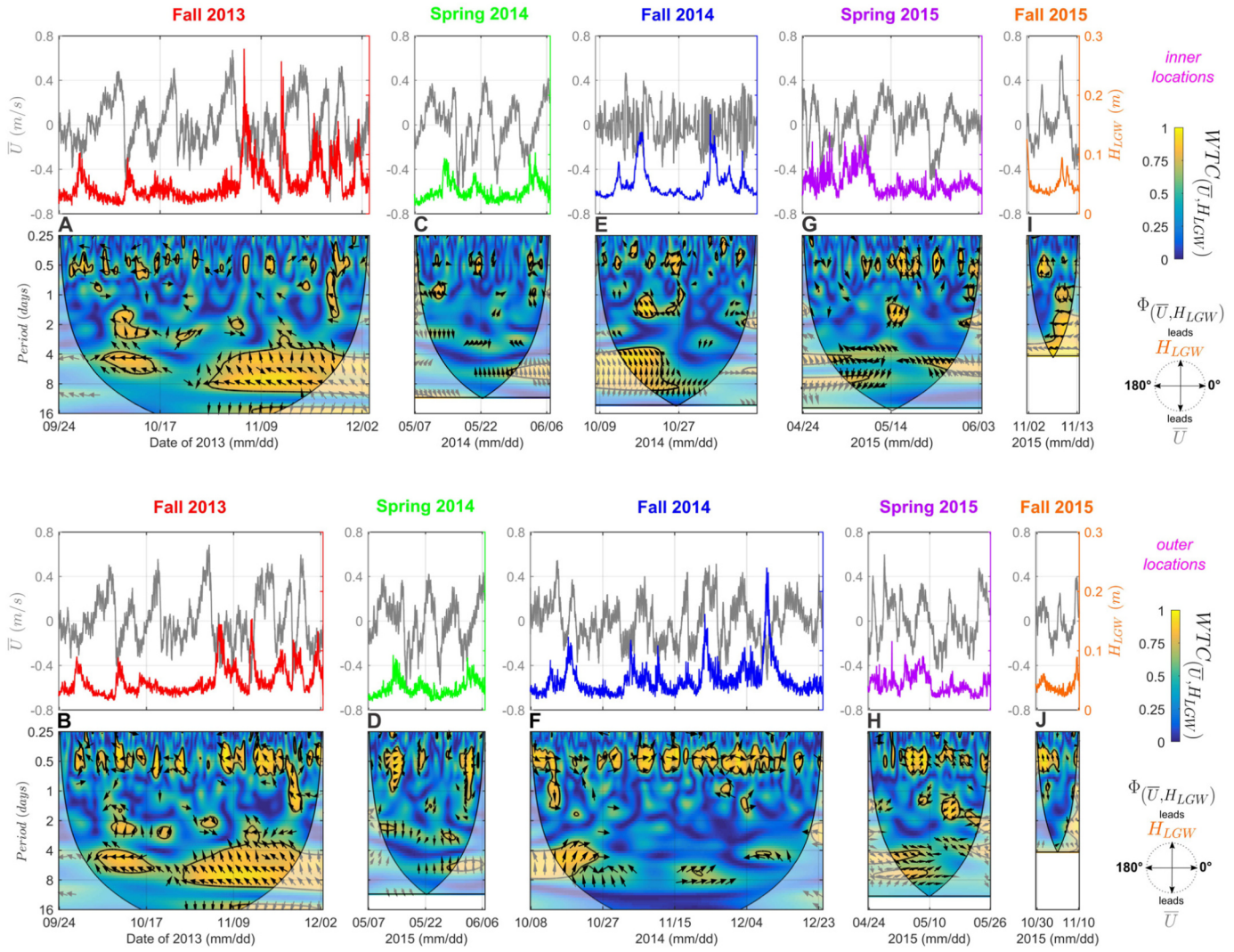

Fig. 7. Time series of $\overline{U}$ (gray) and H_{LGW} (color), and their wavelet coherence spectra and phases, $WTC_{(\overline{U},H_{LGW})}$ and $\Phi_{(\overline{U},H_{LGW})}$, for each deployment and site. See Fig. 5 for the format description.

surfzone width. Two facts translate to smaller LGWs during low tide. First, the level of resonance between triads of waves that include LGWs is inversely proportional to water depth in shallow water. Second, the available space over which transfers occur, i.e. the horizontal extent, is shorter.

Long-gravity waves could also be generated at shoals by the breaking-point forcing mechanism (Symonds et al., 1982). This mechanism is expected to vary according to tidal changes in water depth and bottom profile. If that mechanism operates, larger LGWs should be observed during low tide when steeper profiles and lower depths were expected. That situation, however, does not correspond to our observations.

In contrast to these previous studies, at Cape Canaveral shoals the tidal modulation of LGWs was found to be relatively weak in comparison. Variations in H_{LGW} between successive high and low tides were ~ 0.01 m. This difference may be related to the microtidal regime found near Cape Canaveral (~ 1 m) that might imply small differences in LGW forcing during successive high and low tides.

The fact that coherences between h and H_{LGW} at 2 cycles/day were typically found at outer locations further suggests that isolated shoals exert control on the tidal variability of LGWs. A plausible mechanism relates to a tidal modulation of LGWs that are generated by the shoaling of (and that travel opposite to) short-wave groups (Baldock, 2006; Zou, 2011). In the simplest 2D case, we speculate that the bathymetric profile during low tide has overall wider shoaling and surf zones compared to the high tide profile. This case is different from beaches where typically the surfzone width remains constant over a tidal cycle but the profile shape differs from convex to concave (Thomson et al., 2006).

The refractive trapping of LGWs at shoals (Rijnsdorp et al., 2015) does not explain the phases $\approx 0^{\circ}$ found between h and H_{LGW}. For a given infragravity energy and wavelength, the turning point for shoal-trapped LGWs should migrate offshore during low tide allowing larger energy to reach the deployment locations. This relationship implies larger LGWs during low tide, which was not supported by our observations.

Given that the tidal modulation of LGWs varies with the location in the shoal complex, the interaction between tides and infragravity waves over cape-related shoals may provide a morphodynamic process that contributes to sediment transport gradients at shoals. During times near low tide, relatively weaker tidal flows occur, thus LGW motions and their influence on the cross-shelf exchange would be weaker. The contrary (stronger tidal flows and larger LGWs) would occur during instances close to high tide as suggested by values of $\phi_{(h,\log_{10}[H_{LGW}])}$ between -45 and 45° during Spring 2014, Fall 2014, and Spring 2015 (e.g., Fig. 5D–H). This mechanism would depend upon the direction of LGW transport and resuspension by other processes, e.g. subtidal flows and SGWs. Further observations and analyses can more closely examine this possibility.

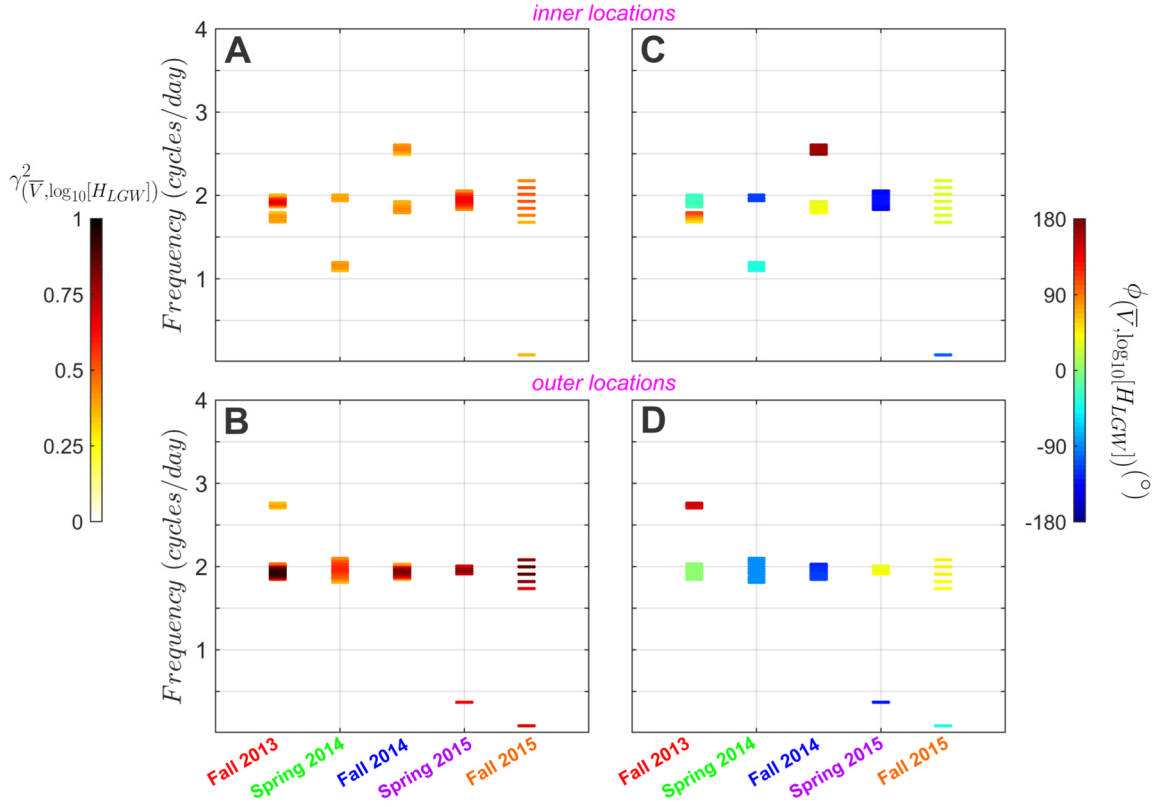

Fig. 8. Scatter plot showing coherence spectra and phases between $\overline{V}$ and $\log_{10}[H_{LGW}]$ at each site of all deployments. See Fig. 4 for details about the formatting.

4.2. Subtidal coherence between flows and LGWs

The coherence between LGWs and flows at subtidal periods can be explained by variations in synoptic processes, namely variations in Florida Current (Gulf Stream measured off South Florida) transport rates and wind speeds. Changes in the strength of the closest western boundary current, the Florida Current (FC), may influence water levels via changes in the cross-shelf pressure gradient that is geostrophically balanced (Pedlosky, 1987). Similarly, wind-driven surface stresses may produce water level tilting and wind-driven flows that are steered by the cape and its complex inner-shelf bathymetry (Lamas et al., 2017). These water elevation changes and horizontally sheared flows likely set the level of triad interactions between SGWs and LGWs, increase the likelihood of short-wave breaking over the shoals, and move the turning point for nearshore trapping of shoreline reflected LGWs (Liu et al., 1990; Herbers et al., 1994; Baldock, 2006; Rijnsdorp et al., 2015).

4.2.1. Coherence between Florida Current transport and LGWs

Fig. 10 shows the time series of FC transport, Q_{FC}, the infragravity wave heights, and their wavelet coherence spectra and phases at the outer locations. During Fall 2013 and Spring 2014 there were two instances of high coherence ($WTC_{(Q_{FC},H_{LGW})}$> 0.75) at 4, 6, and 8 days (bottom panel in Fig. 10A); and 6 days (bottom panel of Fig. 10B), respectively. Phases ranged from 180° to 225° (or − 135°) during Fall 2013, i.e. Q_{FC} leading H_{LGW} by 2–4 days, and from 90° to 135° during Spring 2014, i.e. H_{LGW} leading Q_{FC} by ~ 2 days.

To the best of our knowledge, this connection between geostrophically driven water levels and LGW heights has not been previously explored. However, the role of the Gulf Stream "backset eddies", i.e. vortices formed between the current and shoreline that rotate in the reverse direction to the main current, was recognized more than a century ago as a mechanism that might influence cuspate foreland formation (Gulliver, 1895). In the simplest case, geostrophic flows influence coastal water depths through the relationship (Pond and Pickard, 1995, their Eq. 8.6)

$$f_{Can} V_{FC} = -g\frac{\Delta\eta}{\Delta x}, \tag{7}$$

where V_{FC} is the principal-axis velocity component of the FC, $f_{Can} = 2\Omega \sin(\lambda_{Can})$ ($\approx 6.92 \times 10^{-5}\ s^{-1}$) is the Coriolis frequency at Canaveral shoals with Ω representing the Earth's rotation angular frequency ($\approx 7.27 \times 10^{-5}$ rad/s) and λ_{Can} is the latitude at Canaveral shoals (≈ 28.4°N at Shoal E), g is the acceleration due to gravity, η is the water level, and x is the cross-shelf direction. Values of V_{FC} correspond to $V_{FC} = Q_{FC}/A$, with $A \approx 20 \times 10^6$ m^2 representing approximately half of the cross-sectional area at the submarine cable measurement station in the Straits of Florida (Leaman et al., 1987, their Fig. 2).

If we further assume a uniform water level slope, the variation in water depth at the shoals caused by changes in the Florida Current transport may be given by

$$\Delta\eta \approx \frac{x_{Can} f_{Can} V_{FC}}{g}, \tag{8}$$

with $x_{Can} \approx$ 40 km as a representative distance from the FC to Canaveral shoals. Cross-sectional averaged FC velocities, V_{FC}, thus vary between 1.3 and 1.8 m/s, i.e. Q_{FC} vary between 25 and 35 Sv (Leaman et al., 1987). These observations translate to $\Delta\eta$ ranging from 0.36 to 0.51 m that indicate water level variations of the same order of magnitude as the mean tidal range. Values of $\Delta\eta$ therefore suggest that the coherence between Q_{FC} and H_{LGW} may be related to variations in water level caused by FC transport.

Cross shelf Coriolis accelerations (fv) and gradients in period-averaged normal stresses caused by wave orbital velocities, $\partial S_{xx}/\partial x$, generally balance the cross shelf slope in water elevation as represented by the pressure gradient, $\partial P/\partial x$. In this case, x is the cross shelf direction, v represents the along shelf velocity, P is pressure, and S_{xx} is the cross-

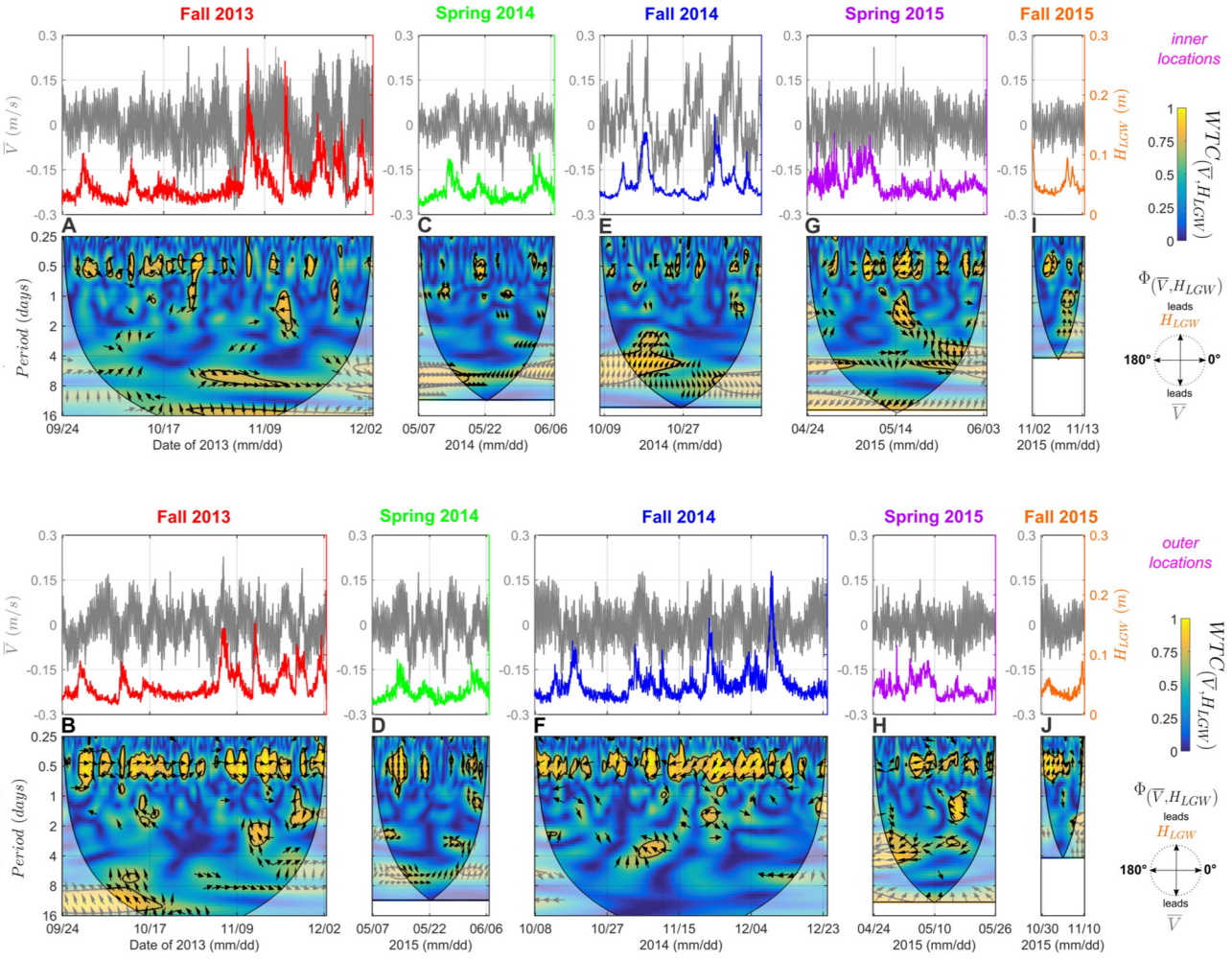

Fig. 9. Time series of $\overline{V}$ (gray) and H_{LGW} (color), and their wavelet coherence spectra and phases, $WTC_{(\overline{V},H_{LGW})}$ and $\Phi_{(\overline{V},H_{LGW})}$, for each deployment and site. The reader is referred to Fig. 5 for details.

shore component of the wave radiation stress normal to the *y*-*z* plane (Lentz et al., 1999). These cross-shelf balances remain not well understood at the transition between the inner shelf and the surfzone, specially over the complicated bathymetry offshore of capes. Possible influences may relate to wave-current interactions among gravity waves propagating in intermediate water depths, horizontally and

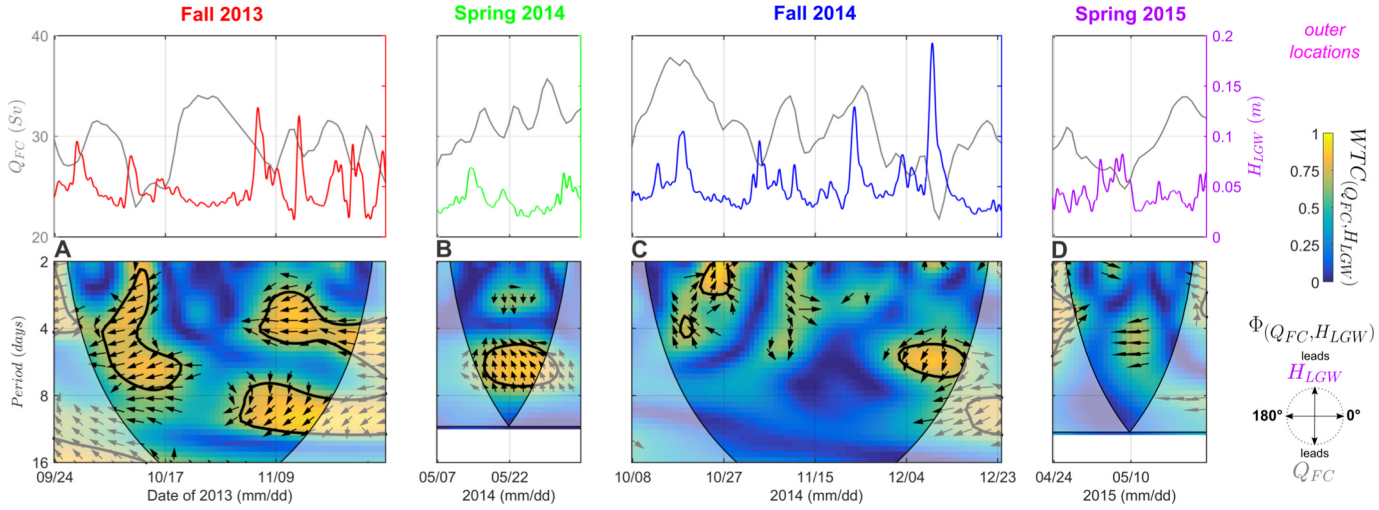

Fig. 10. Time series of the Florida Current transport, Q_{FC} in *Sv* (1 *Sv* = 1×10^6 m^3/s) (gray) and H_{LGW} (color), and their wavelet coherence spectra and phases, $WTC_{(Q_{FC},H_{LGW})}$ and $\Phi_{(Q_{FC},H_{LGW})}$, at the outer location for each deployment. The reader is referred to Fig. 5 for details. The Florida Current transport estimates were made available by the Atlantic Oceanographic and Meteorological Laboratory at www.aoml.noaa.gov/phod/floridacurrent/.

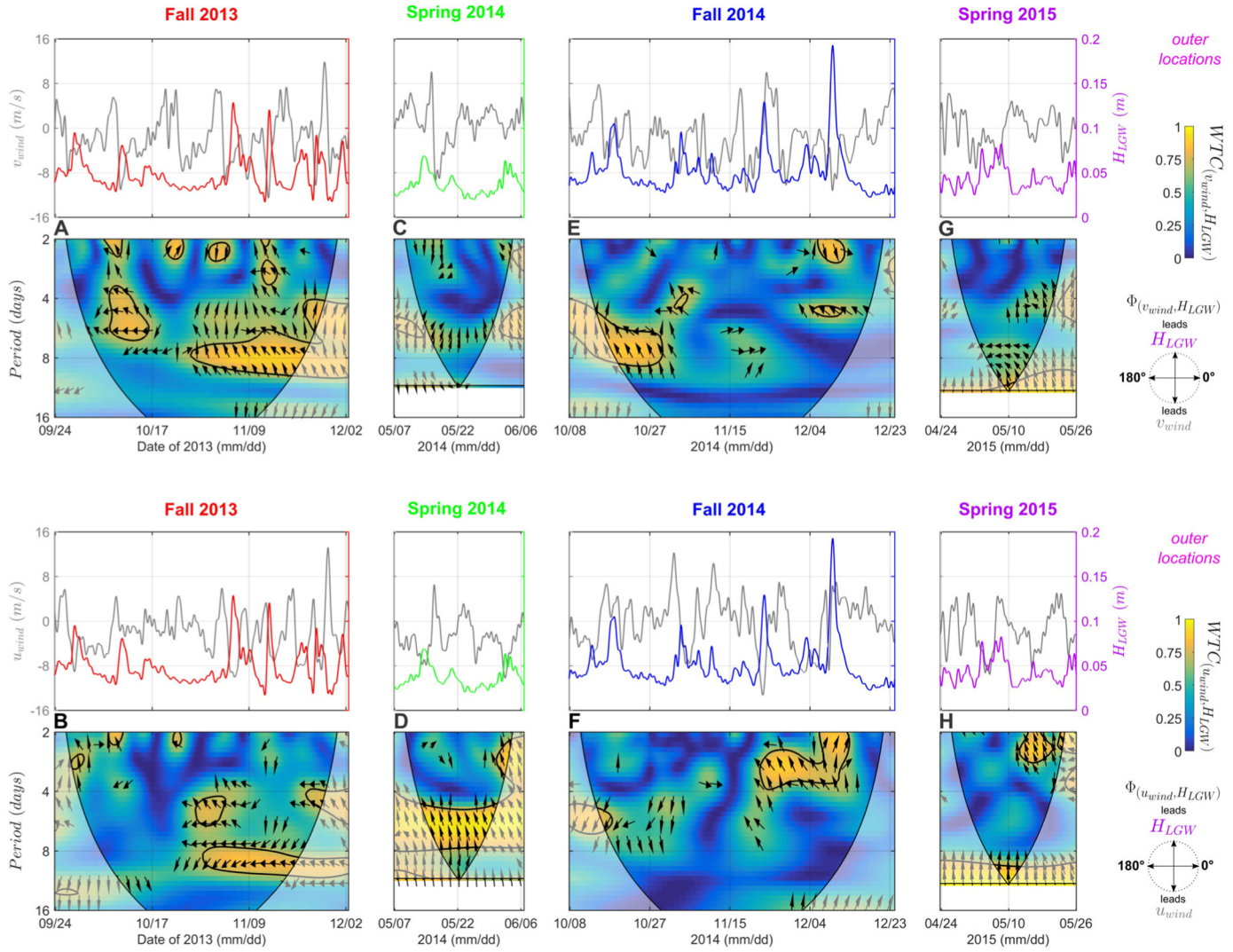

Fig. 11. Time series of the along-shelf (north-south component), v_{wind}, and cross-shelf (east-west component), u_{wind}, both in gray; and H_{LGW} (in color), and their wavelet coherence spectra and phases, $WTC_{(v_{wind},H_{LGW})}$ and $\Phi_{(v_{wind},H_{LGW})}$, at the outer location for each deployment. The reader is referred to Fig. 5 for details. Wind data for the NOAA buoy 41009 are available at http://www.ndbc.noaa.gov/station_page.php?station=41009/.

vertically sheared tidal and subtidal flows, and asymmetries in tidal motions (Lane et al., 2007).

4.2.2. Coherence between offshore wind velocity and LGWs

We separately considered the effects of along- and cross-shelf wind-driven motions on LGWs. Coherence analyses were, therefore, performed between H_{LGW} and the along and cross shelf wind components. These components approximately correspond to the north-south (v_{wind}) and east-west (u_{wind}) wind speed components, respectively.

Upper pairs of subplots (A, C, E, and G) in Fig. 11 show the wavelet coherence spectra and time series for the along-shelf (north-south component) wind speed at an offshore location and infragravity wave heights. High coherence was found during some intervals of Fall 2013 deployment at periods ~ 6–8 days with $\Phi_{(v_{wind},H_{LGW})}$ between 90° and 180° (H_{LGW} leading by ~ 1.5–3 days). High coherence was also found at periods of 8 days during Fall 2014 with $\Phi_{(v_{wind},H_{LGW})} \approx 135°$ (H_{LGW} leading by 3 days) during the ~ 10 day span near 10/27/2014.

Bottom pairs of subplots (B, D, F, and H) in Fig. 11 show the time series of the east-west (cross-shelf) component of wind speeds, u_{wind}; infragravity wave heights; and their wavelet coherence spectra. High coherences, i.e. those larger than 0.75, were found during some instances at periods ranging from 3 to 10 days. During Fall 2013 and Spring 2015 u_{wind} and H_{LGW} were coherent at ~ 10 days with phases ~ 180° (u_{wind} leading by 5 days) during Fall 2013, and 90° (H_{LGW} leading by 2.5 days) during Spring 2015. Note, however, that high coherence during Spring 2015 was found inside the cone of influence most of the time. High coherency was also found during Spring 2014 at a period ~ 6 days with phases ~ 90° (H_{LGW} leading by ~ 1.5 days), and during approximately 20 days near 12/04/2014 at a 3-day period during Fall 2014 with $\Phi_{(u_{wind},H_{LGW})} \approx 135°$ (H_{LGW} leading by 27 h).

Coherences between infragravity waves and water level could be interpreted to be connected to the two synoptic phenomena analyzed, i.e. Florida Current transport and wind speed. During Fall 2013 at periods ~ 8 *days*, $\Phi_{(h,H_{LGW})}$ values were approximately equal to 0° (bottom panel in Fig. 5B), therefore higher water levels were related to larger H_{LGW}. This variability could relate to a modulation of the nonlinear transfers from SGWs to LGWs analogous to the tidal modulation found in the surfzone (Thomson et al., 2006). That connection cannot be explained by relatively larger LGW energy reaching the shoals when water is deeper overall, therefore we suggest subtidal variability was not related to free LGW motions. These ideas are supported by the instances when coherence between H_{LGW} and h was also found between LGWs and Q_{FC} (bottom panels in Fig. 10 A and B), v_{wind} (upper panels in Fig. 11 A), and u_{wind} (bottom panels in Fig. 11 B and D).

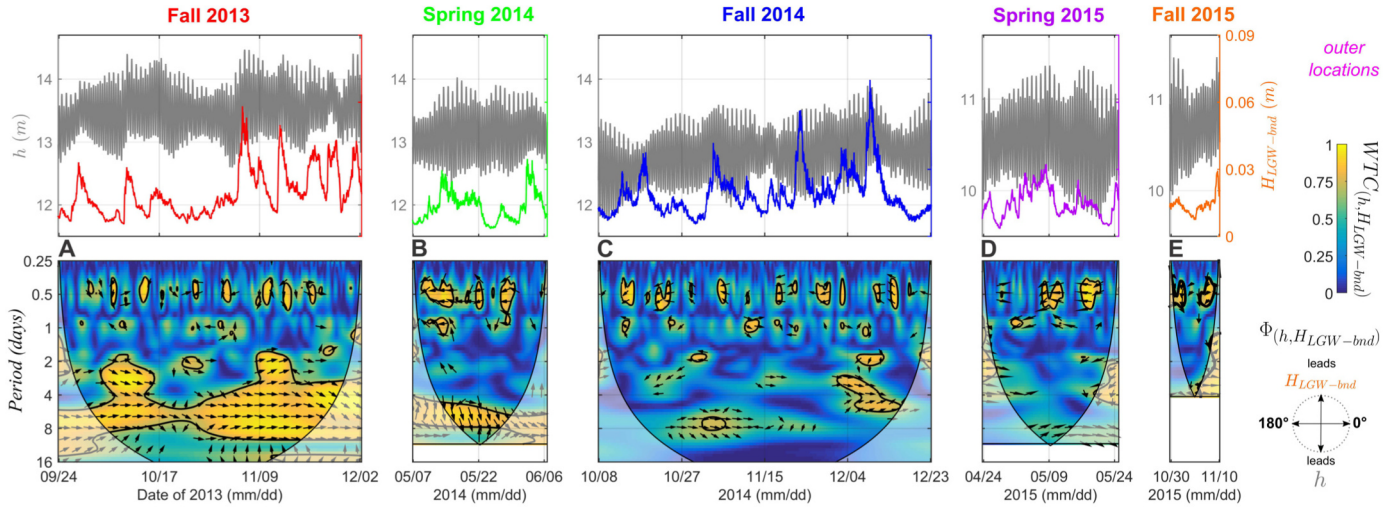

Fig. 12. Time series of h (gray) and bound LGWs heights ($H_{LGW-bnd}$, color), and their wavelet coherence spectra and phases, $WTC_{(h,H_{LGW-bnd})}$ and $\Phi_{(h,H_{LGW})}$, for each deployment at the outer locations. See Fig. 5 for the format description.

4.3. Coherences between water motions and predicted bound LGWs

We calculated the bound (locally forced) infragravity wave heights and analyzed their coherence with ambient flows to identify the processes influencing the former (see Appendix A). Wavelet coherences between bound infragravity wave heights, $H_{LGW-bnd}$, and water levels were inconsistent at tidal frequencies at the outer locations (Fig. 12), but were similar to $WTC_{(h,H_{LGW})}$ at subtidal frequencies in Fall 2013 and Spring 2014. This comparison indicates that triad interactions conducive to bound LGWs generation were sensitive only to variations in subtidal water levels. Similarly, wavelet coherence and phases between bound LGWs and flow conditions, i.e. Q_{FC}, $\overline{U}$, and $\overline{V}$, were similar to their counterparts that included total LGWs.

Wavelet coherences between $H_{LGW-bnd}$, and $\overline{U}$ and $\overline{V}$ are shown in Fig. 13. Low coherence at tidal periodicities, and its (unsteady) occurrence at subtidal frequencies, was observed for $WTC_{(\overline{U},H_{LGW-bnd})}$ (Fig. 13 A, C, E, G, and I). For $WTC_{(\overline{V},H_{LGW-bnd})}$, consistent coherence at tidal frequencies was only observed for ≈ 5 days during Spring 2014 (cf. Fig. 13 B, D, F, H, and J). These observations concur with wavelet coherences between principal-axes motions and H_{LGW} found at outer locations (cf. pairs of subplots B, D, F, H, and J in Figs. 7 and 9).

Fig. 14 shows the wavelet coherence spectra and time series for wind components and bound LGWs heights. Such coherences and phases are comparable to those found between wind components and H_{LGW} (cf. Fig. 11). This comparison suggests that, during some instances, the wind driven motions modulated triad interactions related to bound LGWs. Furthermore, phase values between ~ 135° and 180° indicate that northeastward winds (positive u_{wind} and v_{wind} components) were related to decreasing LGW wave heights, with a temporal lag of ~ 1 day during some occasions. As these phases are also observed between wind and bound LGWs, they suggest that there was a decrease in LGW forcing associated with northeastward winds.

4.4. Coherences between flows and infragravity waves near Capes: implications for the cross-shelf exchange

Cross-shelf sediment transport by LGWs is relatively well represented by the ratio H_{LGW}/H_{SGW} (de Bakker et al., 2016a). In our case, $H_{LGW}/H_{SGW} <$ 0.3 during all deployments, which suggests that our measurements were located in the shoaling zone and LGW-related transport was directed opposite to the direction of SGW propagation (de Bakker et al., 2016a, their Fig. 11a). If we assume LGW transport was directed opposite to the SGW propagation, the LGW-related cross-shelf exchange would depend upon the coherences and phases reported herein. Specifically, the contribution of LGWs to cross-shelf exchange would increase or decrease the net transport depending upon the strength of other processes such as the undertow or the tidal residual currents.

Offshore directed transport linked to SGW-LGW ratio is related to bound infragravity waves (de Bakker et al., 2016a). According to our results, bound LGWs appear to be mostly modulated by subtidal motions, thus offshore-directed transport by LGWs appears to be independent of tidal flows. We expect, however, that the tidally produced residual flow near capes (Geyer, 1993) adds to the subtidally modulated LGW bound motions – possibilities that will be explored in future studies.

Since wind-related subtidal flows typically produce cross-shelf motions, e.g. via Ekman transport, LGWs should enhance, or counteract, sand fluxes depending on the wind direction. Observations exhibiting coherence at ~ 8-day periodicity occurred when wind components were in quadrature with $H_{LGW-bnd}$, with bound infragravity waves leading by ~ 2 days. The fact that wind components were not simultaneously coherent with $H_{LGW-bnd}$ (except during some instances in Fall 2013) suggests northward and eastward (blowing offshore) winds increase SGW-LGW interactions separately.

4.5. Methodological limitations

We acknowledge that our methodology has two weaknesses that could be improved. First, our deployments did not capture the 2-dimensional nature of LGW motions that may include edge waves trapped at shoals similar to bar-trapping at alongshore-uniform bars (Bryan and Bowen, 1996; Rijnsdorp et al., 2015) and alongshore current instabilities (Lippmann et al., 1999). It is conceivable that the shoals are located sufficiently far from the shoreline as to render the alongshore instabilities negligible. However, shore-attached shoals (e.g. Southeast Shoal) may cause the longshore current to migrate offshore as the shoaling zone widens offshore to include isolated shoals. Similarly, the

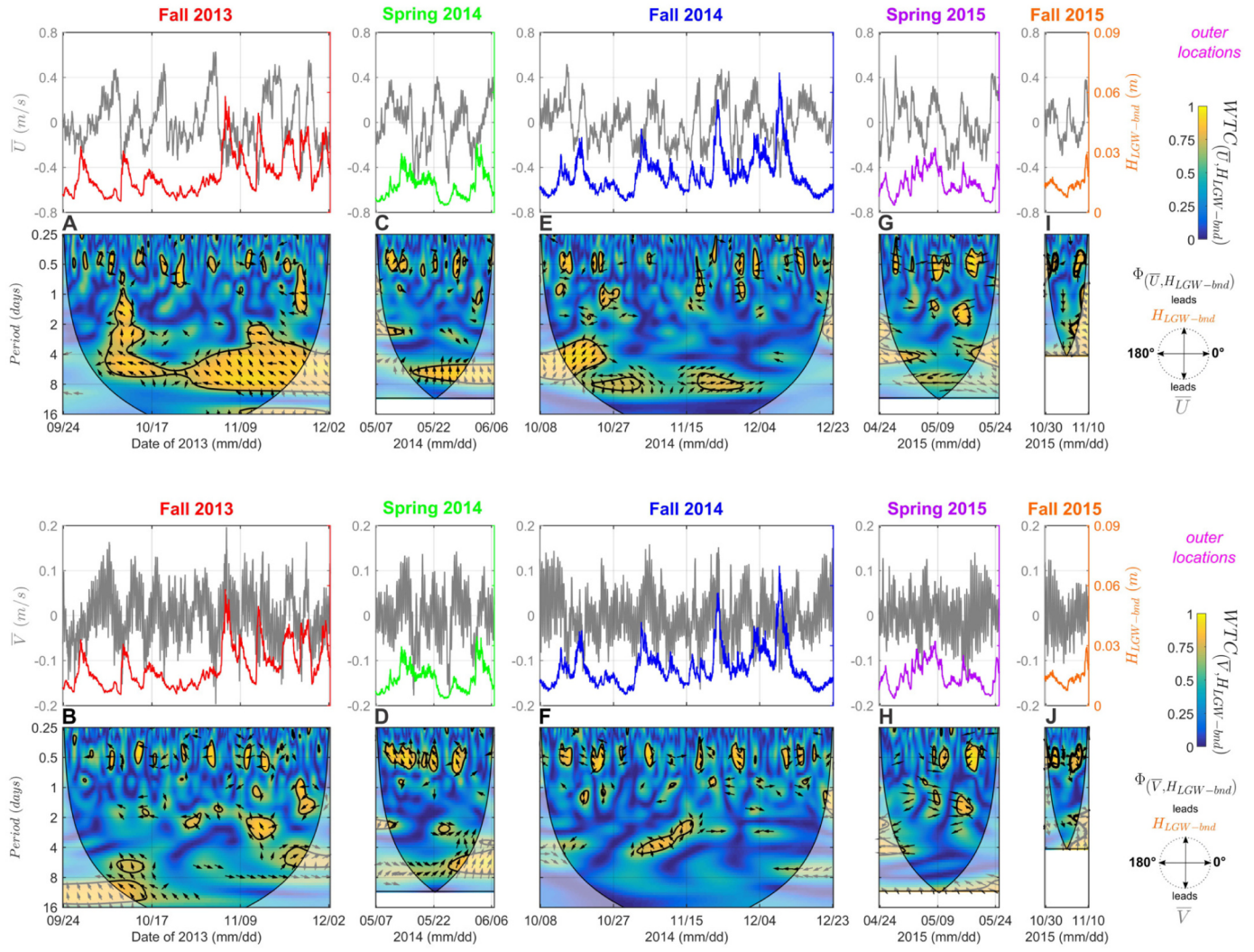

Fig. 13. Time series of $\overline{U}$ and $\overline{V}$ (gray) and bound LGWs heights ($H_{LGW-bnd}$, color), and their wavelet coherence spectra and phases, e.g. $WTC_{(\overline{U},H_{LGW-bnd})}$ and $\Phi_{(\overline{U},H_{LGW})}$, for each deployment at the outer locations. See Fig. 5 for the format description.

shoal-trapping of edge waves (Rijnsdorp et al., 2015) likely governs LGW motions at the shoals. This shortcoming could be addressed by using arrays of instruments at each shoal (Sheremet et al., 2002, 2005) and by applying non-hydrostatic numerical modeling (Rijnsdorp et al., 2015). Second, bound LGW prediction does not account for the effect of horizontally-sheared currents (Liu et al., 1990) or variable depth (Zou, 2011, Section 5). These processes should be relevant offshore of capes as their physiography include the shallow bathymetry of cape shoals and induce flow separation at the inner shelf.

5. Summary and conclusions

Squared coherency and wavelet coherence analyses provided information on the temporal co-variability followed by h, $\overline{U}$, $\overline{V}$, and H_{LGW} at the inner and outer swales of Shoal D and Shoal E, as well as the ridge of Shoal D, near Cape Canaveral, on the Florida Atlantic coast. Statistically significant squared coherencies and wavelet coherences (>0.75) at tidal (~ 2 cycles/day) and subtidal (<2 cycles/day) frequencies were found to be unsteady and heterogeneous at locations within the shoal complex. Semidiurnal coherences were typically found at the outer locations for the total infragravity wave heights. Subtidal coherences were found between ambient flows and bound LGWs regardless of the location.

Cross-shelf particle transport at shoals depends on the coupling of headland-distorted ambient flows, geostrophic water levels and stresses caused by surface gravity waves. These connections include the modulation of triad interactions involving LGWs by water motions driven by the geostrophically balanced Florida Current. The unsteadiness in coherences between LGWs and ambient flows offshore of capes may be linked to morphodynamic feedbacks that govern their evolution over decadal time scales. Although our results did not account for the full range of infragravity motions that may be relevant over the shoals, they do provide evidence of connections among processes that govern cross-shelf exchanges near cuspate forelands.

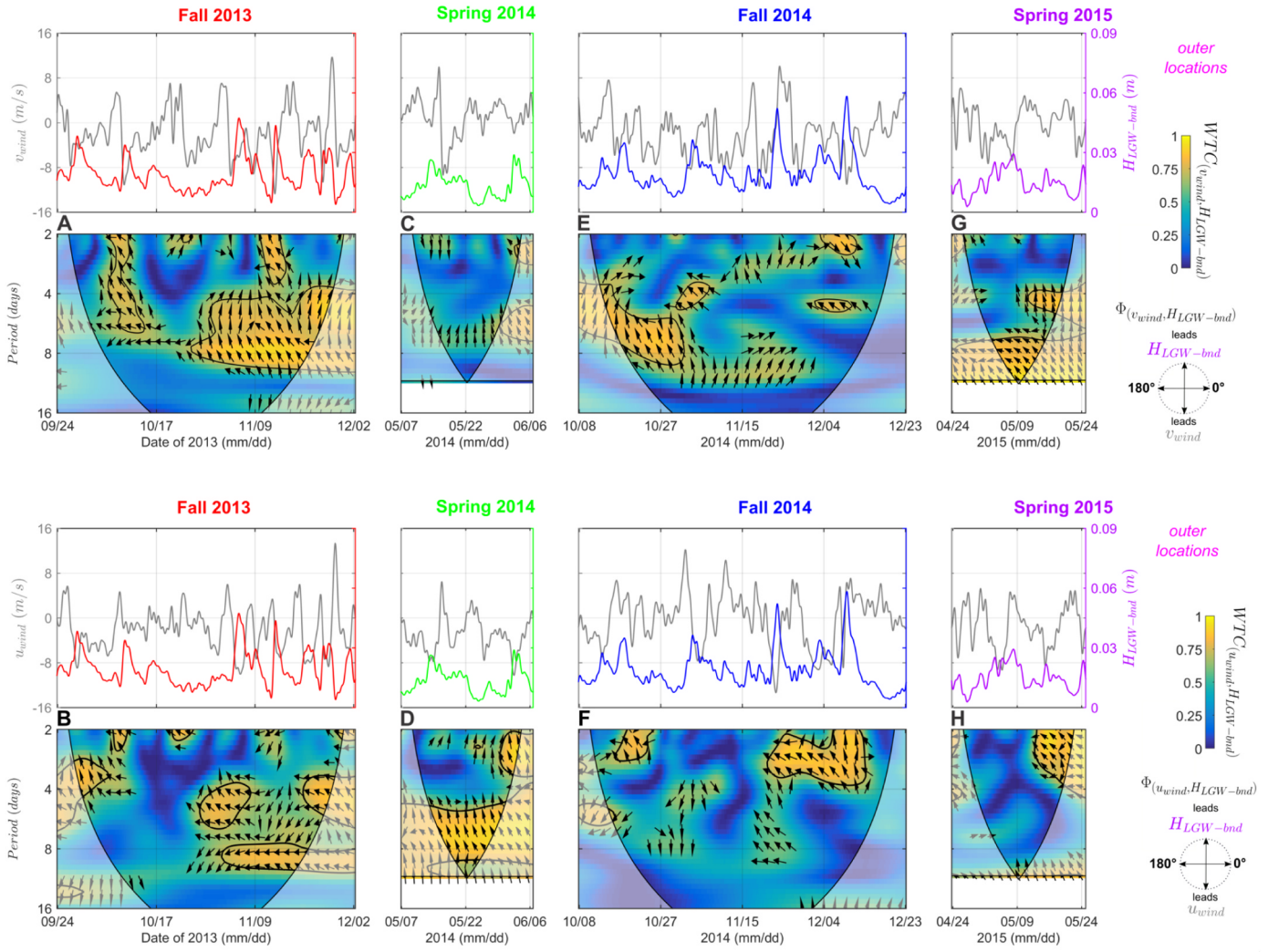

Fig. 14. Time series of east-west u_{wind} and north-south v_{wind} velocity components (gray), and bound LGWs heights ($H_{LGW-bnd}$, in color), and their wavelet coherence spectra and phases, i.e. $WTC_{(u_{wind},H_{LGW-bnd})}$ and $\Phi_{(u_{wind},H_{LGW})}$ for the east-west component, for each deployment at the outer locations. See Fig. 5 for the format description.

Acknowledgements

Study collaboration and funding were provided by the U.S. Department of the Interior, Bureau of Ocean Energy Management, Environmental Studies Program, Washington, DC under Agreement Number M13AC00012. Thanks to Viktor Adams, Michael Dickson, Patrick McGovern, Sangdon So, Lauren Ross, Jackie Branyon, Mohammad Al-Khaldi, Ahmad Yousif, Alessandro Lopes Aguiar, Renan Peixoto Rosario, and all that helped with fieldwork for this project. Discussions with Alex Sheremet, Maitane Olabarrieta, Britt Raubenheimer, Giovanni Coco, and David Clark are greatly appreciated. JFPA acknowledges the support from the Fulbright Commission, the U.S. Department of State, the Ministry of Education of Colombia, University of Florida College of Liberal Arts and Sciences and Department of Geological Sciences, and EAFIT University. SMP acknowledges the support of the American Society for Engineering Education/Naval Research Laboratory Postdoctoral Fellow Program. The Florida Current cable and section data are made freely available on the Atlantic Oceanographic and Meteorological Laboratory web page (www.aoml.noaa.gov/phod/floridacurrent/) and are funded by the DOC-NOAA Climate Program Office - Ocean Observing and Monitoring Division. This manuscript benefited from comments and suggestions of associated editor Prof. Charitha Pattiaratchi and two anonymous reviewers.

Appendix A. Calculating bound infragravity waves

The calculation of bound LGW waves was based on the formalism presented in (Herbers et al. 1994, their Appendix). Also see Sand (1982) and Okihiro et al. (1992). The spectral density of a bound LGW wave of frequency f, $E_{bnd}(f)$, is given by (Herbers et al., 1994, their Eq. A8)

$$E_{bnd}(f) = \int_0^f df' \int_0^{2\pi} d\theta_1 \int_0^{2\pi} d\theta_2 \, D^2(f-f', f', \Delta\theta) E(f-f', \theta_1) E(f', \theta_2) + 2\int_0^{f_{max}} df' \int_0^{2\pi} d\theta_1 \int_0^{2\pi} d\theta_2 \, D^2(f+f', -f', \Delta\theta+\pi) E(f+f', \theta_1) E(f', \theta_2), \quad (A.1)$$

with $E(f', \theta)$ as the directional spectrum at frequency f' and direction θ (Benoit et al., 1997), f_{max}= 0.3 Hz as the maximum frequency in the sea-swell band, and the first and second terms on Eq. (A.1) corresponding to sum and difference interactions, respectively. The interaction coefficient,

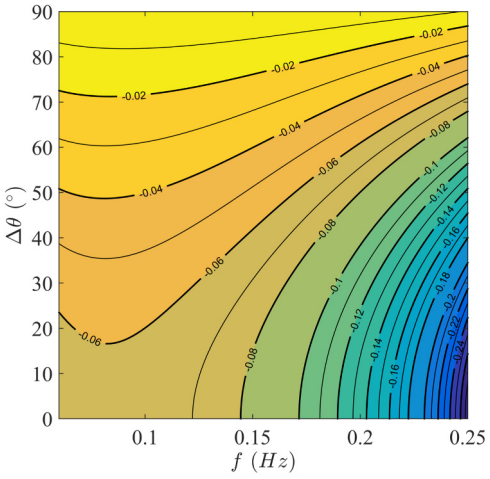

Fig. A.1. Contour plot showing values of the interaction coefficient, $D(f + \Delta f, -f, \Delta\theta + \pi)$, for parameters $h = 13\ m$ and $\Delta f = 0.03\ Hz$ (cf. Herbers et al., 1994, their Fig. 2). (For interpretation of the references to colour in this figure legend, the reader is referred to the web version of this article.)

$D(s_1 f_1, s_2 f_2, \Delta\theta)$, which represents the interaction level between a pair of waves with frequencies f_1 and f_2, and a difference in propagation direction $\Delta\theta$, is given by

$$\begin{aligned} D(s_1 f_1, s_2 f_2, \Delta\theta) = &- \frac{g k_1 k_2 \cos(\Delta\theta)}{2\sigma_1\sigma_2} \\ &+ \frac{g(\sigma_1+\sigma_2)\cosh(k_1 h)\cosh(k_2 h)}{[g k_3 \tanh(k_3 h) - (\sigma_1+\sigma_2)^2]\sigma_1\sigma_2\cosh(k_3 h)} \\ &\times \left\{(\sigma_1+\sigma_2)\left[\left(\frac{\sigma_1\sigma_2}{g}\right)^2 - k_1 k_2 \cos(\Delta\theta)\right]\right. \\ &\left. - 0.5\left[\frac{\sigma_1 k_2^2}{\cosh^2(k_2 h)} + \frac{\sigma_2 k_1^2}{\cosh^2(k_1 h)}\right]\right\}, \end{aligned} \tag{A.2}$$

with i referring to waves 1 and 2, $\sigma_i = 2\pi s_i f_i$, $s_1 = s_2 = 1$ (for sum interactions) or $s_1 = 1$ and $s_2 = -1$ (for difference interactions), and the secondary wavenumber given by $k_3 \equiv |\vec{k_1} + \vec{k_2}| = [k_1^2 + k_2^2 + k_1 k_2 \cos\Delta\theta]^{1/2}$. An example of the coupling coefficient for a given water depth and difference in frequency between the pair with frequencies $f + \Delta f$ and $-f$, $D(f + \Delta f, -f, \Delta\theta + \pi)$, is shown in Fig. A.1. Further, $\vec{k}$ represents the wavenumber in vector form $\vec{k} = (k\cos\theta, k\sin\theta)$, θ is the propagation direction, and $\Delta\theta = \theta_1 - \theta_2$ is the difference in propagation directions of the interacting pair of primary waves $(s_1 f_1, \vec{k_1})$ and $(s_2 f_2, \vec{k_2})$. Note that directions θ_1 and θ_2 relate to the wavenumber via $\vec{k_i} = (k_i\cos\theta_i, k_i\sin\theta_i)$, and f_i relates to k_i, in this case, by the well-known linear dispersion relation (e.g., Guo, 2002)

$$f_i = \frac{1}{2\pi}[g k_i \tanh(k_i h)]^{1/2}. \tag{A.3}$$

Lastly, significant wave heights for the bound (forced) LGWs were calculated as $H_{LGW-bnd} = 4\sqrt{m_{0-bnd}}$, with $m_{0-bnd} = \int_{f_{min}}^{f_{max}} df E_{bnd}$, with $f_{min} = 0.004$ Hz and $f_{max} = 0.05$ Hz. A comparison between H_{LGW} and $H_{LGW-bnd}$ for all deployments is shown in Fig. A.2.

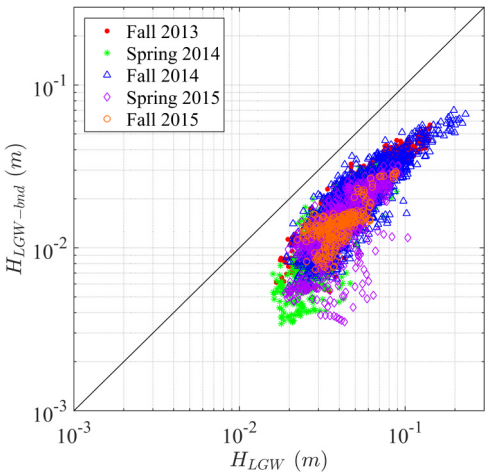

Fig. A.2. Comparison of H_{LGW} and $H_{LGW-bnd}$ for all deployments (cf. Herbers et al., 1994, their Fig. 4b). (For interpretation of the references to colour in this figure legend, the reader is referred to the web version of this article.)

References

Aagaard, T., Greenwood, B., 2008. Infragravity wave contribution to surf zone sediment transport – the role of advection. Mar. Geol. 251, 1–14.

Baldock, T.E., 2006. Long wave generation by the shoaling and breaking of transient wave groups on a beach. Proc. R. Soc. Lond. Ser. A 462, 1853–1876.

Benoit, M., Frigaard, P., Schäffer, H.A., 1997. Analysing multidirectional wave spectra: a tentative classification of available methods. In: Proceedings Seminar on Multidirectional Waves and their Interaction with Structures.

Berthot, A., Pattiaratchi, C., 2006. Mechanisms for the formation of headland-associated linear sandbanks. Cont. Shelf Res. 26, 987–1004.

Bertin, X., de Bakker, A., van Dongeren, A., Coco, G., Andre, G., Ardhuin, F., Bonneton, P., Bouchette, F., Castelle, B., Crawford, W.C., Davidson, M., Deen, M., Dodet, G., Guerin, T., Inch, K., Leckler, F., McCall, R., Muller, H., Olabarrieta, M., Roelvink, D., Ruessink, G., Sous, D., Stutzmann, E., Tissier, M., 2018. Infragravity waves: from driving mechanisms to impacts. Earth-Sci. Rev. 177, 774–799.

Brink, K.H., 2016. Cross-shelf exchange. Annu. Rev. Mar. Sci. 8, 59–78.

Bryan, K.R., Bowen, A.J., 1996. Edge wave trapping and amplification on barred beaches. J. Geophys. Res. 101 (C3), 6543–6552.

de Bakker, A.T.M., Brinkkemper, J.A., van der Steen, F., Tissier, M.F.S., Ruessink, B.G., 2016a. Cross-shore sand transport by infragravity waves as a function of beach steepness. J. Geophys. Res. 121, 554–570.

de Bakker, A.T.M., Tissier, M.F.S., Ruessink, B.G., 2016b. Beach steepness effects on nonlinear infragravity-wave interactions: a numerical study. J. Geophys. Res. 121, 554–570.

Dickey, D.A., Fuller, W.A., 1979. Distribution of the estimators for autoregressive time series with a unit root. J. Am. Stat. Assoc. 74 (366), 427–431. ⟨http://www.jstor.org/stable/2286348⟩.

Dyer, K.R., Huntley, D.A., 1999. The origin, classification and modelling of sand banks and ridges. Cont. Shelf Res. 19, 1285–1330.

Eckart, C., 1951. Surface waves on water of variable depth. Lecture notes, fall semester, 1950-51, Scripps Institution of Oceanography, University of California.

Field, M.E., Duane, D.B., 1974. Geomorphology and sediments of the inner continental shelf, cape canaveral, florida. Technical Memorandum 42, United States Army Corps of Engineers Coastal Engineering Center, USA.

Geyer, W.R., 1993. Three-dimensional tidal flow around headlands. J. Geophys. Res. 98 (January), 955–966.

Grinsted, A., Moore, J.C., Jevrejeva, S., 2004. Application of the cross wavelet transform and wavelet coherence to geophysical time series. Nonlinear Process. Geophys. 11, 561–566.

Gulliver, F.P., 1895. Cuspate forelands. Geol. Soc. Am. Bull. 7, 399–422.

Guo, J., 2002. Simple and explicit solution of wave dispersion equation. Coast. Eng. 45, 71–74.

Herbers, T.H.C., Elgar, S., Guza, R.T., 1994. Infragravity-frequency (0.005–0.05 Hz) motions on the shelf. Part i: forced waves. J. Phys. Oceanogr. 24, 917–927.

Herbers, T.H.C., Elgar, S., Guza, R.T., O'Reilly, W.C., 1995. Infragravity-frequency (0.005–0.05 Hz) motions on the shelf. Part ii: free waves. J. Phys. Oceanogr. 25, 1063–1079.

Holthuijsen, L.H., 2007. Waves in Oceanic and Coastal Waters. Cambridge University Press, Cambridge, UK.

Huntley, D.A., Guza, R.T., Thornton, E.B., 1981. Field observations of surf beat, 1. Progressive edge waves. J. Geophys. Res. 1986 (C7), 6451–6466.

Jenkins, G.M., Priestley, M.B., 1957. The spectral analysis of time series. J. R. Soc. Ser. B (Methodol.) 19 (1), 1–12. ⟨https://www.jstor.org/stable/2983992⟩.

Kumar, N., Voulgaris, G., List, J.H., Warner, J.C., 2013. Alongshore momentum balance analysis on a cuspate foreland. J. Geophys. Res. 118, 5280–5295.

Lamas, L., Peliz, A., Dias, J., Oliveira, P.B., Angelico, M.M., Castro, J.J., Fernandes, J.N., Trindade, A., Cruz, T., 2017. Diurnal variability of inner-shelf circulation in the lee of a cape under upwelling conditions. Cont. Shelf Res. 143, 67–77.

Lane, E.M., Restrepo, J.M., McWilliams, J.C., 2007. Wave-current interaction: a comparison of radiation-stress and vortex-force representations. J. Phys. Oceanogr. 37, 1122–1141.

Leaman, K.D., Molinari, R.L., Vertes, P.S., 1987. Structure and variability of the Florida Current at 27n: April 1982–July 1984. J. Phys. Oceanogr. 17, 565–583.

Lentz, S., Guza, R.T., Elgar, S., Feddersen, F., Herbers, T.H.C., 1999. Momentum balance on the North Carolina inner shelf. J. Geophys. Res. 104 (C8), 18205–18226.

Lentz, S.J., Fewings, M.R., Howd, P.A., Fredericks, J., Hathaway, K., 2008. Observations and a model of undertow over the inner continental shelf. J. Phys. Oceanogr. 38, 2341–2357.

Limber, P.W., Adams, P.P.N., Murray, A.B., 2017. Modeling large-scale shoreline change caused by complex bathymetry in low-angle wave climates. Mar. Geol. 383, 55–64.

Lippmann, T.C., Herbers, T.H.C., Thornton, E.B., 1999. Gravity and shear wave contributions to nearshore infragravity motions. J. Phys. Oceanogr. 29, 231–239.

Liu, P.L.-F., Dingemans, M.W., Kostense, J.K., 1990. Long-wave generation due to the refraction of short-wave groups over a shear current. J. Phys. Oceanogr. 20, 53–59.

Longuet-Higgins, M.S., Stewart, R.W., 1962. Radiation stress and mass transport in gravity waves, with application to surf beats. J. Fluid Mech. 13, 481–504.

McNinch, J.E., Luettich Jr, R.A., 2000. Physical processes around a cuspate foreland: implications to the evolution and long-term maintenance of a cape-associated shoal. Cont. Shelf Res. 20.

Nittrouer, C.A., Wright, L.D., 1994. Transport of particles across continental shelves. Rev. Geophys. 32 (1), 85–113.

Okihiro, M., Guza, R.T., 1995. Infragravity energy modulation by tides. J. Geophys. Res. 100 (C8), 16,143–16,148.

Okihiro, M., Guza, R.T., Seymour, R.J., 1992. Bound infragravity waves. J. Geophys. Res. 97 (C7), 11,453–11,469.

Olsen Associates, I., 2013. Brevard County, Florida, Federal Shore Protection Project, South Reach, 2010 Project Renourishment, 3-Year Post-Construction Monitoring of the Canaveral Shoals II Offshore Borrow Area (June 2013). Tech. rep. Olsen Associates, Inc., FL.

Paniagua-Arroyave, J.F., Adams, P.N., Valle-Levinson, A., Parra, S.M., 2018. Infragravity wave heights and ambient motions at cape canaveral shoals. Data Set Mendeley Data (⟨10.17632/kmk7ngcbwb.1⟩).

Pedlosky, J., 1987. Geophysical Fluid Dynamics. Springer-Verlag, New York, NY, USA.

Pomeroy, A., Lowe, R., Symonds, G., van Dongeren, A., Moore, C., 2012. The dynamics of infragravity wave transformation over a fringing reef. J. Geophys. Res. 117 (C11022), 1–17.

Pond, S., Pickard, G.L., 1995. Introductory Dynamical Oceanography, 2nd edition. Butterworth Heinmann, Oxford, UK.

Rijnsdorp, D.P., Ruessink, G., Zijlema, M., 2015. Infragravity-wave dynamics in a barred coastal region, a numerical study. J. Geophys. Res. 120, 1–22.

Ruessink, B.G., Houwman, K.T., Hoekstra, P., 1998. The systematic contribution of transporting mechanisms to the cross-shore sediment transport in water depths of 3–9 m. Mar. Geol. 152, 295–324.

Sand, S.E., 1982. Long waves in directional seas. Coast. Eng. 6, 195–208.

Sheremet, A., Guza, R.T., Elgar, S., Herbers, T.H., 2002. Observations of nearshore infragravity waves: seaward and shoreward propagating components. J. Geophys. Res. 107 (C8), 3095. https://doi.org/10.1029/2001JC000970.

Sheremet, A., Guza, R.T., Herbers, T.H.C., 2005. A new estimator for directional properties of nearshore waves. J. Geophys. Res. 110, 1–11.

Signell, R.P., Geyer, W.R., 1990. Transient eddy formation around headlands. J. Geophys. Res. 96 (C2), 2561–2575.

Symonds, G., Huntley, D.A., Bowen, A.J., 1982. Two-dimensional surf beat: long wave generation by a time-varying breakpoint. J. Geophys. Res. 87 (C1), 492–498.

Thieler, E.R., Foster, D.S., Himmelstoss, E.A., Mallinson, D.J., 2014. Geologic framework of the northern north carolina, USA inner continental shelf and its influence on coastal evolution. Mar. Geol. 348, 113–130.

Thompson, D.M., Plant, N.G., Hansen, M.E., 2015. Analysis of Bathymetric Surveys to Identify Coastal Vulnerabilities at Cape Canaveral, Florida (Open File Report 2015-1180). U.S. Geological Survey https://doi.org/10.3133/ofr20151180.

Thomson, J., Elgar, S., Herbers, T.H.C., 2005. Reflection and tunneling of ocean waves observed at a submarine canyon. Geophys. Res. Lett. 32 (L10602), 1–4.

Thomson, J., Elgar, S., Raubenheimer, B., Herbers, T.H.C., Guza, R.T., 2006. Tidal modulation of infragravity waves via nonlinear energy losses in the surfzone. Geophys. Res. Lett. 33 (L05601).

Thomson, R.E., Emery, W.J., 2014. Data Analysis Methods in Physical Oceanography. Elsevier B.V., Waltham, MA, USA.

Torrence, C., Compo, G.P., 1998. A practical guide to wavelet analysis. Bull. Am. Meteorol. Soc. 79 (1), 61–78.

Torrence, C., Webster, P.J., 1999. Interdecadal changes in the enso-monsoon system. J. Clim. 12, 2679–2690.

Winter, G., Lowe, R.J., Symonds, G., Hansen, J.E., van Dongeren, A.R., 2017. Standing infragravity waves over an alongshore irregular rocky bathymetry. J. Geophys. Res. 122, 4868–4885.

Zou, Q., 2011. Generation, transformation, and scattering of long waves induced by a short-wave group over finite topography. J. Phys. Oceanogr. 41, 1842–1859.